A phase-field description for mixed-mode fracture propagation

Meng Fan[1,2], Yan Jin[1], and Thomas Wick[2]

[1]State Key Laboratory of Petroleum Resources and Prospecting, China University of Petroleum, 102249 Beijing, China

[2]Institut für Angewandte Mathematik, Leibniz Universität Hannover, Welfengarten 1, 30167 Hannover, Germany

Abstract

The goal of this work is to develop a phase-field fracture model capable of capturing mixed-mode fracture propagation behavior. In nature, failure of rocks and rock-like materials is usually accompanied by the propagation of mixed-mode fractures. To address this problem, some recent studies have incorporated mixed-mode fracture propagation criteria to the classic phase-field fracture model and proposed new energy splitting methods to split the total crack driving energy into mode-I and mode-II parts. But these new models have sometimes the shortcomings of being not numerically-robust or not physically sound. From a numerical viewpoint, they are all solved with staggered solution schemes. In this work, an existing energy splitting method for masonry-like materials is modified and incorporated into the phase-field model for mixed-mode fractures. A fully-monolithic scheme is used to solve the model. Therein, a primal-dual active set method is employed for treating the fracture irreversibility. Moreover, our computational framework uses adaptive mesh refinement of a predictor-corrector type and parallel computing to reduce the computation time. Three numerical tests are carried out, and the results of the new model are compared to those of existing models, demonstrating the numerical robustness and physical soundness of the new model. In total, six splitting methods are compared and computationally analyzed.

Keywords: phase-field fracture; mixed-mode fracture; uniaxial compression test; finite elements; predictor-corrector mesh refinement

1 Introduction

In classical fracture mechanics, three fundamental modes of fractures are defined. They are termed as tensile (mode-I), in-plane shear (mode-II) and anti-plane shear (mode-III) respectively [5]. But the fractures we deal with in reality are mostly mixed-mode. For example, mixed mode-I and mode-II fracture propagation is very common in rocks under compression [27, 10]. Because of its complex formation mechanism and propagation path, simulation of mixed-mode fracture requires the extension of classical Griffith' theory [16] and the incorporation of robust numerical method.

In [28], the maximum strain energy release rate criterion (G-criterion) is modified and a F-criterion for mixed-mode fracture propagation is proposed. In recent studies [32, 8], this criterion is incorporated into the phase-field fracture model, which is known for its capability to capture complex fracture behavior such as branching, coalescence, and three-dimensional propagation. The crack driving energy in the original phase-field formulation is split into mode-I and mode-II parts. This is achieved by splitting the crack driving stress σ^+ into σ_I^+ and σ_{II}^+, or in some cases, splitting crack driving strain e^+ into e_I^+ and e_{II}^+. In [32], the energy splitting method for single-mode fractures [25] is modified so that the first and second terms of σ^+ correspond to σ_I^+ and σ_{II}^+ respectively. This method can distinguish primary cracks from secondary cracks in uniaxially-compressed limestones, but it overestimates the maximum force response when mode-I loading is dominant. More physically-sound splitting methods are proposed in [30, 29] [1], where the tension-compression asymmetry of the normal stress on fracture surfaces is fulfilled explicitly. However, how to determine fracture surface direction remains unsolved in these two works. In [8], a similar splitting method is derived based on the tension-compression asymmetry of the normal strain on fracture surfaces. And the direction of fracture surface is determined by solving a local fracture dissipation maximization problem. In some numerical experiments we have carried out, the latter three splitting methods are not numerically robust. Newton iteration steps increase sharply when the crack starts to propagate and in some cases divergence takes place. In [14], a splitting method for masonry-like materials is derived based on structured deformation theory under the principal strain coordinate. This method has a similar formulation to those in [30, 29], but is more robust. However, it can only deal with mode-I fracture as there is no mode-II fracture driving energy term in its formulation.

In this work, our goal is to design a phase-field model for mixed-mode fracture descriptions. Phase-field methods and variational formulations of fracture propagation have seen a tremendous popolarity in the last years; starting with the models proposed in [13, 7]. Therein, two equations are coupled: a displacement model and a phase-field function. The latter is a regularized equation with a model parameter ϵ that characterizes the thickness of a smoothed transition zone from full fracture to the unbroken material.

We follow the ideas in [8, 14] and develop a physically-sound and numerically-robust phase-field splitting method which can be used to treat mixed-mode fractures. This method is incorporated into the mixed-mode phase-field fracture formulation in [32]. Specifically, we propose to change the

[1] Although these two papers are not aimed at solving mixed-mode fracture problem, the proposed splitting methods are capable of splitting σ^+ into σ_I^+ and σ_{II}^+

reference frame of the energy splitting method proposed in [14] from principal strain coordinates to local fracture surface coordinates, so that the crack-driving energy is further split into mode-I crack driving part and mode-II crack driving part. The fracture surface direction is determined based on the maximum-dissipation criterion from [8]. We further develop a simpler computational algorithm as derived in Section 3.6.

The resulting phase-field model is implemented based on the framework developed in [17, 18], which is capable of parallel computations and uses adaptive mesh refinement employing a predictor-corrector scheme in order to detect the a priori unknown fracture path. Three numerical tests are carried out under different mesh sizes h and transitional zone sizes ϵ, and the results of our new model are compared with those of the existing models. These comparisons demonstrate the numerical robustness and physical soundness of our new model. Preliminary results of this work are published in [12].

The outline of this paper is as follows: In Section 2 the notation and governing equations for mixed-mode phase-field fracture model are presented. Next in Section 3 several energy splitting methods for mixed-mode fractures are reviewed and our new splitting method is derived. In Section 4 the detailed algorithm and numerical scheme used to solve our model are presented. Then in Section 5 three numerical tests based on five existing splitting methods and our new splitting method are presented and analyzed. Finally in Section 6 contents of this paper are summarized and conclusions are drawn.

2 Governing Equations for Mixed-Mode Phase-Field Fracture Models

2.1 Notation

In this subsection, we introduce the basic notation used in the paper. Let $B \subset \mathbb{R}^2$ denote the whole two-dimensional domain, inside which a lower-dimensional sharp crack $C \subset \mathbb{R}$ exists. Following [7], a phase-field variable $\varphi \in [0, 1]$ is introduced, where $\varphi = 0$ represents the fully-damaged state and $\varphi = 1$ the undamaged state. Then C is approximated using $\Omega_F \subset B$ with the help of elliptic functional proposed in [3, 2]. The boundary of the regularized fracture is denoted as $\partial\Omega_F$, whose position is dependent on the characteristic length ϵ. Now the entire domain can be divided into the intact part $\Omega_I \subset B$ and the fractured part Ω_F. More specifically:

$$\Omega_I := \{x \in B \mid \varphi(x) = 1\} \tag{1}$$

$$\Omega_F := \{x \in B \mid \varphi(x) < 1\}. \tag{2}$$

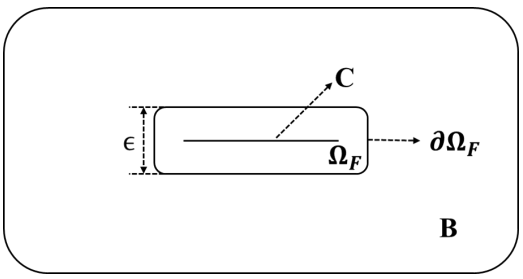

Figure 1: Geometric setting notation of phase-field fracture model

Fig. 1 gives an illustration of the geometric setting notation. After applying Dirichlet boundary condition on the domain outer boundary ∂B, we are now faced with a two-field problem depending on the displacement $u : B \to \mathbb{R}^2$ and phase-field variable $\varphi : B \to [0, 1]$. Finally, we denote the L^2 scalar product: (1) for vectors, $(m, n) := \int_B m \cdot n dx$; (2) for second-order tensors, $(M, N) := \int_B M : N dx$.

2.2 Governing equations

In this subsection, we start with the original phase-field fracture model and then introduce its evolvement into the mixed-mode phase-field fracture model.

In [13], Griffith's theory is generalized to form a variational approach capable of treating crack nucleation, initiation and growth. In [7], a phase-field variable is introduced to numerically solve the model. In [26] and [4], thermodynamically-consistent phase-field fracture models are proposed in which energy is split into fracture-driving and non-fracture-driving parts. Based on the aforementioned literatures, the governing equations for thermodynamically-consistent phase-field fracture model can be constructed starting from the energy functional $E(u, \varphi)$:

$$\begin{aligned} E(u,\varphi) \;=\; & \frac{1}{2}\left((1-\kappa)\,\varphi^2+\kappa\right)\left(\sigma^+(u), e(u)\right) + \frac{1}{2}\left(\sigma^-(u), e(u)\right) \\ & + \frac{G_c}{2}\left(\frac{1}{\epsilon}(1-\varphi, 1-\varphi) + \epsilon\,(\nabla\varphi, \nabla\varphi)\right), \end{aligned} \tag{3}$$

where G_c is the critical energy release rate, and κ is a small numerical parameter to prevent singularity in Jacobian matrix. $e(u)$ denotes Cauchy strain. $\sigma^+(u)$ and $\sigma^-(u)$ denote the crack-driving and non-crack driving stresses respectively, and they are fully partitioned from the total stress $\sigma(u)$:

$$\sigma(u) \;=\; \sigma^+(u) + \sigma^-(u). \tag{4}$$

The material is assumed to be linear-elastic:

$$\sigma(u) \;=\; \lambda \mathrm{tr}(e(u))\, I + 2\mu e(u), \tag{5}$$

where λ and μ are Lam*é* coefficients. Since we are dealing with two-dimensional cases in this paper, we want to emphasize that λ has different formulations in plane stress and plane strain settings:

$$\lambda \;=\; \frac{E\nu}{(1+\nu)(1-\nu)} \quad \text{in plane stress setting} \tag{6}$$

$$\lambda \;=\; \frac{E\nu}{(1+\nu)(1-2\nu)} \quad \text{in plane strain setting,} \tag{7}$$

while μ has the same formulation in both settings:

$$\mu \;=\; \frac{E}{2(1+\nu)}, \tag{8}$$

where E denotes Young's modulus and ν denotes Poisson's ratio.

To determine the crack propagation path, we need to find the u and φ which minimize $E(u, \varphi)$. In the meantime, an inequality constraint must be enforced so that crack irreversibility is fulfilled. For the following, let us introduce three function spaces: Let $V := \left(H_0^1(B)\right)^2$, $W := H^1(B)$, $W_{in} := \left\{\varphi \in W \mid \varphi \le \varphi^{n-1} \le 1 \text{ a.e. on } \Omega\right\}$.

This minimization problem with inequality constraint can be described as:

Formulation 2.1. *Let the time step sequence be denoted by the index $n = 0, 1, 2, \cdots$. Find vector-valued displacements $u := u^n \in \{u_D + V\}$ and a scalar-valued phase-field variable $\varphi := \varphi^n \in W_{in}$ such that:*

$$min\ E(u, \varphi) \quad s.t.\ \varphi \leq \varphi^{n-1}. \tag{9}$$

The variational form of the constrained minimization problem in Formulation 2.1 constitutes the governing equations for phase-field fracture model by differentiating $E(u, \varphi)$ with respect to u and φ:

Formulation 2.2. *Let the time step sequence be denoted by the index $n = 0, 1, 2, \cdots$. With u^0 and φ^0 as the initial conditions, at each following time step t^n, find the displacement and phase-field variables $\{u, \varphi\} := \{u^n, \varphi^n\} \in \{u_D + V\} \times W_{in}$ by solving:*

$$\begin{aligned} &\frac{1}{2}\left((1-\kappa)\varphi^2 + \kappa\right)\left(\left(\sigma^+(u), e(w)\right) + \left(\sigma^+(w), e(u)\right)\right) \\ &+\frac{1}{2}\left(\left(\sigma^-(u), e(w)\right) + \left(\sigma^-(w), e(u)\right)\right) = 0 \qquad\qquad \forall w \in V, \end{aligned} \tag{10}$$

and

$$\begin{aligned} &(1-\kappa)\varphi\left(\sigma^+(u) : e(u), \psi - \varphi\right) \\ &+G_c\left(-\frac{1}{\epsilon}(1-\varphi, \psi-\varphi) + \epsilon\left(\nabla\varphi, \nabla(\psi-\varphi)\right)\right) \geq 0 \quad \forall \psi \in W \cap L^\infty. \end{aligned} \tag{11}$$

Here $u_D := u_D(t)$ is the prescribed Dirichlet boundary condition at each time step. However, when treating mixed mode-I and mode-II fractures, Eq. (11) should be modified so that both G_{Ic} and G_{IIc} instead of just G_c are incorporated into the governing equations. This modification is inspired by [28], where the crack propagation criterion for single-mode fracture, namely G-criterion:

$$\text{crack propagates when:} \quad G \geq G_c, \tag{12}$$

is modified and a F-criterion accounting for mixed-mode fracture is proposed:

$$\text{crack propagates when:} \quad \max_{\theta \in [-\pi, \pi)} F(\theta) \geq 1, \tag{13}$$

where

$$F(\theta) = \frac{G_I(\theta)}{G_{Ic}} + \frac{G_{II}(\theta)}{G_{IIc}}. \tag{14}$$

Here θ denotes the angle between the current crack surface direction and the crack propagation direction. In [32, 8], the F-criterion is incorporated into Eq. (10) and (11), and the phase-field model for mixed-mode fractures is proposed:

Formulation 2.3. *With u^0 and φ^0 as the initial conditions, at each incremental time step $n = 1, 2, 3\cdots$, find the displacement and phase-field variables $\{u, \varphi\} := \{u^n, \varphi^n\} \in \{u_D + V\} \times W_{in}$ by solving:*

$$\begin{aligned} &\frac{1}{2}\left((1-\kappa)\varphi^2 + \kappa\right)\left(\left(\sigma_I^+(u) + \sigma_{II}^+(u), e(w)\right) + \left(\sigma_I^+(w) + \sigma_{II}^+(w), e(u)\right)\right) \\ &+\frac{1}{2}\left(\left(\sigma^-(u), e(w)\right) + \left(\sigma^-(w), e(u)\right)\right) = 0 \qquad\qquad \forall w \in V, \end{aligned} \tag{15}$$

and

$$(1-\kappa)\,\varphi\left(\left(\frac{\sigma_I^+(u)}{G_{Ic}}+\frac{\sigma_{II}^+(u)}{G_{IIc}}\right):e(u),\psi-\varphi\right)$$
$$+\left(-\frac{1}{\epsilon}(1-\varphi,\psi-\varphi)+\epsilon(\nabla\varphi,\nabla(\psi-\varphi))\right)\geq 0\quad\forall\psi\in W\cap L^\infty. \tag{16}$$

The remaining problem is how to determine the mode-I crack driving stress σ_I^+ and mode-II crack driving stress σ_{II}^+.

3 Stress Splitting Methods for Mixed-Mode Phase-Field Fracture Models

In this section, we first review several stress splitting methods that have been proposed in the literature. Then, we introduce our modifications in order to obtain a numerically-robust and physically-sound method.

3.1 Stress Splitting à la Miehe et al. [25]

The stress splitting method proposed in [25] is widely used in phase-field fracture models. The crack-driving and non-crack-driving stresses are defined as:

$$\sigma^+ = \lambda <\mathrm{tr}(e)> I + 2\mu e^+, \tag{17}$$
$$\sigma^- = \lambda(\mathrm{tr}(e)- <\mathrm{tr}(e)>)I + 2\mu(e-e^+), \tag{18}$$

with

$$e^+ = Pe_p^+P^T \tag{19}$$
$$e_p^+ = \begin{pmatrix} <e_{p1}> & 0 \\ 0 & <e_{p2}> \end{pmatrix}, \tag{20}$$

where e_{p1} and e_{p2} are eigenvalues of strain tensor e, and matrix P consists of normalized eigenvectors.

In [32], σ_I^+ and σ_{II}^+ are directly extracted from Eq. (17):

$$\sigma_I^+ = \lambda <\mathrm{tr}(e)> I \tag{21}$$
$$\sigma_{II}^+ = 2\mu e^+. \tag{22}$$

As it is already pointed out in [32], this splitting method has the disadvantage of overestimating the maximum force response under tension-dominant loading. We can give an illustration of this disadvantage via a simple example. Assuming an element at the fracture tip is subjected to uniaxial tension stress σ_{xx} in the x direction, the strain state of the element can be described as:

$$e = \begin{pmatrix} e_{xx} & 0 \\ 0 & -\nu e_{xx} \end{pmatrix}. \tag{23}$$

In this case, the crack driving energy should be pure mode-I, i.e. $\sigma_I^+ : e > 0$ and $\sigma_{II}^+ : e = 0$. But if the previous splitting method is used, we obtain $\sigma_{II}^+ : e = 2\mu(e_{xx})^2$, which is even comparable to $\sigma_I^+ : e = (1-\nu^2)\lambda(e_{xx})^2$. If the studied material has $G_{IIc} > G_{Ic}$, this method will underestimate the crack driving energy and thus overestimate the force response.

3.2 Stress Splitting à la Amor et al. [4]

Another widely used stress splitting method is proposed in [4]. In this method, the crack crack-driving and non-crack-driving stresses are defined as:

$$\sigma^+ = \lambda <\mathrm{tr}(e)> I + 2\mu e_D \tag{24}$$

$$\sigma^- = \lambda(\mathrm{tr}(e) - <\mathrm{tr}(e)>)I, \tag{25}$$

with

$$e_D = e - \frac{1}{d}\mathrm{tr}(e)I, \tag{26}$$

where d is the dimension number of the studied case, which in this paper equals 2.

Inspired by [32], we can also heuristically extract σ_I^+ and σ_{II}^+ from Eq. (24):

$$\sigma_I^+ = \lambda <\mathrm{tr}(e)> I \tag{27}$$

$$\sigma_{II}^+ = 2\mu e_D. \tag{28}$$

We again use the uniaxial tension setting to test this modified splitting method. In this case, $\sigma_{II}^+ : e = (1+\nu)^2\mu(e_{xx})^2$, which is comparable to $\sigma_I^+ : e = (1-\nu)^2\lambda(e_{xx})^2$. Therefore, this method also has a force overestimation problem if the studied material has the property $G_{IIc} > G_{Ic}$.

3.3 Stress splitting à la Strobl/Seelig [30] and Steinke/Kaliske [29]

The splitting methods proposed in [30, 29] do not have the overestimation problem. These two methods, although the former is presented in the strain form and the latter is presented in the stress form, are basically the same. They are both derived under the local crack coordinates and both have the assumptions that:

- The fracture can sustain compressive, but not tensile, normal stress perpendicular to its surface.
- The fracture cannot sustain shear stress tangential to its surface, i.e. the fracture surface is frictionless.

For the convenience of implementation, we only present the strain-form formulation in [30]. In 2D case, let $\boldsymbol{n}$ and $\boldsymbol{s}$ denote the directions normal and tangential to the fracture surface respectively. Their formulation reads:

$$\begin{aligned}
\boldsymbol{\sigma_I^+} &= \boldsymbol{\lambda}\mathrm{tr}(\boldsymbol{e_I^+})\boldsymbol{I} + \boldsymbol{2\mu e_I^+} \\
\boldsymbol{\sigma_{II}^+} &= \boldsymbol{\lambda}\mathrm{tr}(\boldsymbol{e_{II}^+})\boldsymbol{I} + \boldsymbol{2\mu e_{II}^+} \\
\boldsymbol{\sigma^-} &= \boldsymbol{\lambda}\mathrm{tr}(\boldsymbol{e^-})\boldsymbol{I} + \boldsymbol{2\mu e^-},
\end{aligned} \tag{29}$$

where

$$\boldsymbol{e_I^+} = \begin{cases} \begin{pmatrix} \boldsymbol{e_{nn} + \frac{\lambda}{\lambda+2\mu} e_{ss}} & \boldsymbol{0} \\ \boldsymbol{0} & \boldsymbol{0} \end{pmatrix} & \text{if } \boldsymbol{e_{nn} + \frac{\lambda}{\lambda+2\mu} e_{ss} > 0}, \\ \boldsymbol{0} & \text{if } \boldsymbol{e_{nn} + \frac{\lambda}{\lambda+2\mu} e_{ss} \leq 0}. \end{cases} \tag{30}$$

$$\boldsymbol{e_{II}^+} = \begin{pmatrix} \boldsymbol{0} & \boldsymbol{e_{ns}} \\ \boldsymbol{0} & \boldsymbol{0} \end{pmatrix} \tag{31}$$

$$\boldsymbol{e^- = e - e_I^+ - e_{II}^+}. \tag{32}$$

We again use the uniaxial tension example to test this splitting method. If the fracture propagation direction is perpendicular to the uniaxial loading , which is a fair assumption in homogeneous isotropic material, then $\boldsymbol{e_{II}^+ = 0}$, $\boldsymbol{\sigma_{II}^+ = 0}$, and correspondingly $\boldsymbol{\sigma_{II}^+(u) : e(u) = 0}$. Therefore, this splitting method does not have the overestimation problem in uniaxial tension test. However in our experiment, this method is not numerically robust as the Newton iteration step has a sharp increase when crack starts to propagate and sometimes divergence takes place. The reason for this is not fully clear yet. But the singular strain tensors in Eq. (30) and (31) might lead to a large condition number in the local Jacobian matrix and thus have a bad influence on the global Jacobian matrix. Consequently, the nonlinear and linear solvers show bad convergence histories.

3.4 Stress Splitting à la Bryant/Sun [8]

In [8], a similar splitting method is derived based on the assumptions that:

- The fracture can sustain compressive, but not tensile, normal strain perpendicular to its surface.
- The fracture surface cannot sustain shear strain tangential to its surface.

Although this method is presented in energy-form in [8], it is presented here in an equivalent strain-form so that the differences between different splitting methods are more clear:

$$\boldsymbol{e_I^+} = \begin{cases} \begin{pmatrix} \boldsymbol{e_{nn}} & \boldsymbol{0} \\ \boldsymbol{0} & \boldsymbol{0} \end{pmatrix} & \text{if } \boldsymbol{e_{nn} \geq 0}, \\ \boldsymbol{0} & \text{if } \boldsymbol{e_{nn} < 0}. \end{cases} \tag{33}$$

$$\boldsymbol{e_{II}^+} = \boldsymbol{\frac{1}{2}} \begin{pmatrix} \boldsymbol{0} & \boldsymbol{e_{ns}} \\ \boldsymbol{e_{sn}} & \boldsymbol{0} \end{pmatrix}. \tag{34}$$

Then $\boldsymbol{\sigma_I^+}$ and $\boldsymbol{\sigma_{II}^+}$ are calculated using Eq. (29). This method, similar to the ones in [30, 29], can address the uniaxial example well, but is not numerically robust.

3.5 Stress Splitting à la Freddi/Royer-Carfagni [14]

In [14], an energy splitting method is derived based on the structural strain theory under principal strain coordinates. Its assumption is that the structured, or non-elastic, part of the strain can be represented by a symmetric positive-semidefinite tensor. Let $\boldsymbol{p1}$ denotes the direction of the eigenvector

corresponding to the most-positive eigenvalue. And $\boldsymbol{p2}$ denotes the direction of the other eigenvector. The method's formulation reads:

$$\boldsymbol{e}^{+} = \begin{cases} \begin{pmatrix} \boldsymbol{e_{p1}} & \boldsymbol{0} \\ \boldsymbol{0} & \boldsymbol{e_{p2}} \end{pmatrix} & \text{if } \boldsymbol{e_{p2} > 0}, \\ \begin{pmatrix} \boldsymbol{e_{p1}} + \frac{\boldsymbol{\lambda}}{\boldsymbol{\lambda+2\mu}}\boldsymbol{e_{p2}} & \boldsymbol{0} \\ \boldsymbol{0} & \boldsymbol{0} \end{pmatrix} & \text{if } \boldsymbol{e_{p2} \leq 0} \text{ and } \boldsymbol{e_{p1} + \frac{\lambda}{\lambda+2\mu}e_{p2} > 0}, \\ \boldsymbol{0} & \text{if } \boldsymbol{e_{p1} + \frac{\lambda}{\lambda+2\mu}e_{p2} \leq 0}. \end{cases} \tag{35}$$

Eq. (35) is very similar to Eq. (30) if $\boldsymbol{p1}$ and $\boldsymbol{n}$ coincide. It can also be inferred that Eq. (35) is numerically more robust than Eq. (30). Because in the most "dangerous" case where both principal strains are positive, the crack driving strain tensor $\boldsymbol{e}^{+}$ is not singular anymore. This inference will be verified by the numerical test results in Section 5. This splitting method can capture the tensile fracture geometry under compression loading [15]. But it does not account for mixed-mode fractures, as there is only $\boldsymbol{e}^{+}$ instead of $\boldsymbol{e}_{\boldsymbol{I}}^{+}$ and $\boldsymbol{e}_{\boldsymbol{II}}^{+}$ in the formulation.

3.6 Our Stress Splitting Model

Therefore, we do a heuristic modification to the last splitting method. More specifically, the reference frame is changed from the principal strain coordinate to the local crack coordinate, and $\boldsymbol{e}_{\boldsymbol{I}}^{+}$ and $\boldsymbol{e}_{\boldsymbol{II}}^{+}$ are determined to account for mixed-mode fractures. The new formulation reads:

$$\boldsymbol{e}_{\boldsymbol{I}}^{+} = \begin{cases} \begin{pmatrix} \boldsymbol{e_{nn}} & \boldsymbol{0} \\ \boldsymbol{0} & \boldsymbol{e_{ss}} \end{pmatrix} & \text{if } \boldsymbol{e_{nn} + \frac{\lambda}{\lambda+2\mu}e_{ss} > 0} \text{ and } \boldsymbol{e_{ss} > 0}, \\ \begin{pmatrix} \boldsymbol{e_{nn}} + \frac{\boldsymbol{\lambda}}{\boldsymbol{\lambda+2\mu}}\boldsymbol{e_{ss}} & \boldsymbol{0} \\ \boldsymbol{0} & \boldsymbol{0} \end{pmatrix} & \text{if } \boldsymbol{e_{nn} + \frac{\lambda}{\lambda+2\mu}e_{ss} > 0} \text{ and } \boldsymbol{e_{ss} \leq 0}, \\ \boldsymbol{0} & \text{if } \boldsymbol{e_{nn} + \frac{\lambda}{\lambda+2\mu}e_{ss} \leq 0}, \end{cases} \tag{36}$$

$$\boldsymbol{e}_{\boldsymbol{II}}^{+} = \frac{\boldsymbol{1}}{\boldsymbol{2}} \begin{pmatrix} \boldsymbol{0} & \boldsymbol{e_{ns}} \\ \boldsymbol{e_{sn}} & \boldsymbol{0} \end{pmatrix}. \tag{37}$$

Again, $\boldsymbol{\sigma}_{\boldsymbol{I}}^{+}$ and $\boldsymbol{\sigma}_{\boldsymbol{II}}^{+}$ are calculated using Eq. (29). As for the fracture surface direction, we refer to [8] to solve an additional local dissipation maximization problem. Let $\boldsymbol{\theta}$ denote the angle between $\boldsymbol{n}$ and $\boldsymbol{p1}$, we define the normalized crack driving energy as:

$$\boldsymbol{F}(\boldsymbol{u}, \boldsymbol{\theta}) = \left(\frac{\boldsymbol{\sigma}_{\boldsymbol{I}}^{+}(\boldsymbol{u}, \boldsymbol{\theta})}{\boldsymbol{G_{Ic}}} + \frac{\boldsymbol{\sigma}_{\boldsymbol{II}}^{+}(\boldsymbol{u}, \boldsymbol{\theta})}{\boldsymbol{G_{IIc}}} \right) : \boldsymbol{e}(\boldsymbol{u}), \tag{38}$$

then the normal direction of crack surface can be determined by:

$$\boldsymbol{\theta_n} = \mathrm{Arg}\{ \max_{\boldsymbol{\theta} \in [\boldsymbol{0}, \frac{\boldsymbol{\pi}}{\boldsymbol{2}})} \boldsymbol{F}(\boldsymbol{u}, \boldsymbol{\theta}) \}. \tag{39}$$

After a simple derivation, we obtain:

$$\frac{\partial \boldsymbol{F}(\boldsymbol{u},\boldsymbol{\theta})}{\partial \boldsymbol{\theta}} = \begin{cases} \boldsymbol{\mu}\left(\boldsymbol{e_{p1}}-\boldsymbol{e_{p2}}\right)^{\mathbf{2}}\left(\dfrac{\mathbf{1}}{\boldsymbol{G_{IIc}}}-\dfrac{\mathbf{2}}{\boldsymbol{G_{Ic}}}\right)\sin 4\boldsymbol{\theta} & \text{if } \boldsymbol{e_{nn}}+\frac{\boldsymbol{\lambda}}{\boldsymbol{\lambda}+2\boldsymbol{\mu}}\boldsymbol{e_{ss}}>\mathbf{0} \text{ and } \boldsymbol{e_{ss}}>\mathbf{0}, \\ \boldsymbol{\mu}\left(\boldsymbol{e_{p1}}-\boldsymbol{e_{p2}}\right)^{\mathbf{2}}\left(\dfrac{\mathbf{1}}{\boldsymbol{G_{IIc}}}-\dfrac{\mathbf{1}}{\boldsymbol{G_{Ic}}}\right)\sin 4\boldsymbol{\theta} & \\ -\dfrac{(\boldsymbol{\lambda}+2\boldsymbol{\mu})\left(\boldsymbol{e_{p1}^2}-\boldsymbol{e_{p2}^2}\right)}{\boldsymbol{G_{Ic}}}\sin 2\boldsymbol{\theta} & \text{if } \boldsymbol{e_{nn}}+\frac{\boldsymbol{\lambda}}{\boldsymbol{\lambda}+2\boldsymbol{\mu}}\boldsymbol{e_{ss}}>\mathbf{0} \text{ and } \boldsymbol{e_{ss}}\leq\mathbf{0}, \\ \dfrac{\boldsymbol{\mu}\left(\boldsymbol{e_{p1}}-\boldsymbol{e_{p2}}\right)^{\mathbf{2}}}{\boldsymbol{G_{IIc}}}\sin 4\boldsymbol{\theta} & \text{if } \boldsymbol{e_{nn}}+\frac{\boldsymbol{\lambda}}{\boldsymbol{\lambda}+2\boldsymbol{\mu}}\boldsymbol{e_{ss}}\leq\mathbf{0}. \end{cases} \tag{40}$$

In all three situations, the local maximum points of $\boldsymbol{F}(\boldsymbol{u},\boldsymbol{\theta})$ are located at $\boldsymbol{\theta}=\mathbf{0}$ or $\boldsymbol{\theta}=\frac{\boldsymbol{\pi}}{\mathbf{4}}$ or both. Therefore, instead of implementing complicated global maximum search algorithm, we can compare $\boldsymbol{F}(\boldsymbol{u},\mathbf{0})$ and $\boldsymbol{F}(\boldsymbol{u},\frac{\boldsymbol{\pi}}{\mathbf{4}})$ and choose the $\boldsymbol{\theta}$ that maximizes $\boldsymbol{F}(\boldsymbol{u},\boldsymbol{\theta})$ as $\boldsymbol{\theta_n}$. The details about the implementation will be presented in Section 4.4.

4 Finite-Element Implementation and Solution Algorithms

In this section we first briefly introduce our spatial discretization strategy. Then we introduce a primal-dual active set method used to treat crack irreversibility. This approach can be characterized as a semi-smooth Newton method ([19]) is then combined with a classical Newton technique resulting in a combined Newton algorithm [17, 18]. Then our specific forms of the Newton residual and the Jacobian matrix are presented. Finally, the detailed algorithm for implementing our new splitting method is presented.

4.1 Spatial Discretization

A Galerkin finite element method is used to spatially discretize the 2D domain. Quadrilateral elements with bilinear shape functions ($\boldsymbol{Q_1}$) for both $\boldsymbol{u}$ and $\boldsymbol{\varphi}$ are used. Consequently, we work with the discrete spaces $\boldsymbol{V_h}\subset\boldsymbol{V}$, $\boldsymbol{W_h}\subset\boldsymbol{W}$ and $\boldsymbol{W_{inh}}\subset\boldsymbol{W_{in}}$. For the locally adapted meshes, we work with hanging nodes; see e.g. [9].

4.2 Primal-Dual Active Set Method and a Combined Newton Algorithm

In this subsection, we follow closely [17] and recapitulate the main steps for Newton's method solving an unconstrained minimization problem. To this end, the primal-dual active set method is used to treat crack irreversibility and the final algorithm which combines the former two methods into one iteration at each time step.

4.2.1 Newton's method for a minimization problem

First, we rewrite Formulation 2.1 into a more compact form:

$$\min \boldsymbol{E}(\boldsymbol{U}), \tag{41}$$

$$\text{subject to } \boldsymbol{U} \leq \bar{\boldsymbol{U}} \text{ on } \boldsymbol{\Phi} := \boldsymbol{0} \times \boldsymbol{W}, \tag{42}$$

where $\boldsymbol{U} \in \{\boldsymbol{u_D} + \boldsymbol{V}\} \times \boldsymbol{W_{in}}$ is the solution of current time step, and $\bar{\boldsymbol{U}}$ is the solution from last time step.

The unconstrained minimization problem in Eq. (41) can be solved using Newton's method. A Newton iteration sequence $\boldsymbol{U^0}, \boldsymbol{U^1}, \ldots, \boldsymbol{U^N}$ can be constructed in each time step, with

$$\boldsymbol{U^{k+1}} = \boldsymbol{U^k} + \boldsymbol{\delta U^k}, \tag{43}$$

where the update $\boldsymbol{\delta U^k}$ is computed as the solution of the linear system:

$$\boldsymbol{\nabla^2 E(U^k) \delta U^k} = -\boldsymbol{\nabla E(U^k)}, \tag{44}$$

if at each Newton iteration step, the condition

$$\boldsymbol{\delta U^k} \leq \boldsymbol{0} \quad \text{on } \boldsymbol{\Phi}, \tag{45}$$

is fulfilled, and let the initial guess $\boldsymbol{U^0} = \bar{\boldsymbol{U}}$, then the crack irreversibility constraint in Eq. (42) can be fulfilled since $\boldsymbol{U^{k+1}} = \boldsymbol{U^k} + \boldsymbol{\delta U^k} \leq \boldsymbol{U^k} \leq \cdots \boldsymbol{U^0} = \bar{\boldsymbol{U}}$ on $\boldsymbol{\Phi}$.

4.2.2 A primal-dual active set method

In the following, the notation is shorten by dropping the index $\boldsymbol{k}$ of Newton iteration, i.e. $\boldsymbol{\delta U} := \boldsymbol{\delta U^k}$, and setting $\boldsymbol{G} := \boldsymbol{\nabla^2 E(U^k)}$, $\boldsymbol{F} := -\boldsymbol{\nabla E(U^k)}$. Thus the system described by Eq. (44) and Eq. (45) can be rewritten as a minimization problem:

$$\min\left(\tfrac{\boldsymbol{1}}{\boldsymbol{2}}(\boldsymbol{\delta U}, \boldsymbol{G\delta U}) - (\boldsymbol{F}, \boldsymbol{\delta U})\right), \quad \text{with } \boldsymbol{\delta U} \leq \boldsymbol{0} \text{ on } \boldsymbol{\Phi}. \tag{46}$$

Following [19] the minimization problem Eq. (46) can be solved using a primal-dual active set strategy. Using a Lagrange multiplier $\boldsymbol{\lambda} \in \boldsymbol{0} \times \boldsymbol{W^*}$ (where $\boldsymbol{W^*}$ is the dual space of $\boldsymbol{W}$), the minimization problem can be described using a equation system:

$$(\boldsymbol{G\delta U}, \boldsymbol{Z}) + (\boldsymbol{\lambda}, \boldsymbol{Z}) = (\boldsymbol{F}, \boldsymbol{Z}) \quad \forall \boldsymbol{Z} \in \boldsymbol{V} \times \boldsymbol{W}, \tag{47}$$

$$\boldsymbol{C}(\boldsymbol{\delta U}, \boldsymbol{\lambda}) = \boldsymbol{0}, \tag{48}$$

where

$$\boldsymbol{C}(\boldsymbol{\delta U}, \boldsymbol{\lambda}) = \boldsymbol{\lambda} - \boldsymbol{\max}(\boldsymbol{0}, \boldsymbol{\lambda} + \boldsymbol{c\delta U}) \quad \text{with } \boldsymbol{\delta U} \in \boldsymbol{\Phi}, \tag{49}$$

for a given $\boldsymbol{c} > \boldsymbol{0}$. The primal-dual active set strategy replaces the condition $\boldsymbol{C}(\boldsymbol{\delta U}, \boldsymbol{\lambda}) = \boldsymbol{0}$ with $\boldsymbol{\delta U} = \boldsymbol{0}$ on $\boldsymbol{\Phi}$ in the active set $\boldsymbol{\mathcal{A}}$ and $\boldsymbol{\lambda} = \boldsymbol{0}$ in the inactive set $\boldsymbol{\mathcal{I}}$. In other words, the active set is the subdomain where the constraint is applied and no PDE is solved. The inactive set is the subdomain where constraint is already fulfilled and PDE is solved. The algorithm for computing active set reads:

Algorithm 4.1. *In each time step, with* $\boldsymbol{\delta U^0}$ *and* $\boldsymbol{\lambda^0}$ *as initial condition, repeat for* $\boldsymbol{k = 1, 2, \cdots}$ *until the active set* $\boldsymbol{\mathcal{A}^k}$ *does no longer change:*

1. Compute active set:

$$\begin{aligned} \boldsymbol{\mathcal{A}^k} &= \left\{ \boldsymbol{x} \mid \boldsymbol{\lambda^{k-1}(x) + c\delta U^{k-1}(x) > 0} \right\}, \\ \boldsymbol{\mathcal{I}^k} &= \left\{ \boldsymbol{x} \mid \boldsymbol{\lambda^{k-1}(x) + c\delta U^{k-1}(x) \leq 0} \right\}. \end{aligned} \tag{50}$$

2. Compute $\boldsymbol{\delta U^k \in V \times W}$ *and* $\boldsymbol{\lambda^k \in 0 \times W^*}$ *using:*

$$\begin{aligned} \boldsymbol{(G\delta U^k, Z) + (\lambda^k, Z)} &= \boldsymbol{(F, Z)} && && \boldsymbol{\forall Z \in V \times W}, \\ \boldsymbol{(\delta U^k, \psi)} &= \boldsymbol{0} && \textit{on } \boldsymbol{\mathcal{A}^k} && \boldsymbol{\forall \psi \in 0 \times \{W \cap L^\infty\}}, \\ \boldsymbol{\lambda^k} &= \boldsymbol{0} && \textit{on } \boldsymbol{\mathcal{I}^k}. \end{aligned} \tag{51}$$

A discretized version of step 2 leads to a linear system with block structure:

$$\begin{pmatrix} \boldsymbol{G} & \boldsymbol{B} \\ \boldsymbol{B^T} & \boldsymbol{0} \end{pmatrix} \begin{pmatrix} \boldsymbol{\delta U_h^k} \\ \boldsymbol{\lambda_h^k} \end{pmatrix} = \begin{pmatrix} \boldsymbol{F} \\ \boldsymbol{0} \end{pmatrix}. \tag{52}$$

By using quadrature only on the support points of $\boldsymbol{\lambda_h^k}$, $\boldsymbol{B}$ becomes diagonal. The equations $\boldsymbol{B^T \delta U_h^k = 0}$ is not actually solved, but handled via linear constraints used to eliminate equations in the $\boldsymbol{G}$ block on active set $\boldsymbol{\mathcal{A}^k}$. The eliminated equations are those where the $\boldsymbol{i}$-th entry of $\boldsymbol{\lambda_h^k}$ is non-zero. Therefore, the linear equation system simplifies to:

$$\boldsymbol{\hat{G}\delta U_h^k = \hat{F}}, \tag{53}$$

where $\boldsymbol{\hat{G}}$ and $\boldsymbol{\hat{F}}$ stem from $\boldsymbol{G}$ and $\boldsymbol{F}$ by removing the constrained rows from the system.

Finally, each entry of $\boldsymbol{\lambda_h^k}$ can be computed using:

$$\boldsymbol{(\lambda_h^k)_i = (B^{-1})_{ii} \left(F - G\delta U_h^k \right)_i}. \tag{54}$$

Then, $\boldsymbol{\lambda_h^k}$ is used to compute the active set $\boldsymbol{\mathcal{A}^{k+1}}$. The index $\boldsymbol{i}$ is in the active set $\boldsymbol{\mathcal{A}^{k+1}}$ if

$$\boldsymbol{(\lambda_h^k)_i + c(\delta U_h^k)_i > 0}, \tag{55}$$

and in the inactive set $\boldsymbol{\mathcal{I}^{k+1}}$ otherwise.

4.2.3 A combined semi-smooth Newton solver

In the implementation, two Newton iterations, namely the active set computation iteration and the PDE solving iteration, are combined into one iteration to calculate the variable $\boldsymbol{\delta U^k}$. The combined iteration contains a back-tracking line search to improve the convergence radius. Moreover, Eq. (55) is rewritten using the earlier notation:

$$\boldsymbol{(B^{-1})_{ii}(-\nabla E_\epsilon(U_h^k) - \nabla^2 E_\epsilon(U_h^k)\delta U_h^k)_i + c(\delta U_h^k)_i > 0}, \tag{56}$$

and the linear residual $\boldsymbol{-\nabla E_\epsilon(U_h^k) - \nabla^2 E_\epsilon(U_h^k)\delta U_h^k}$ is replaced by the non-linear residual $\boldsymbol{R(U_h^{k+1}) = -\nabla E_\epsilon(U_h^{k+1})}$. Finally, the algorithm combining two iterations can be described as:

Algorithm 4.2. *In each time step, with* $\boldsymbol{U^0}$, $\boldsymbol{\delta U^0}$ *and* $\boldsymbol{\lambda^0}$ *as initial conditions, repeat for* $\boldsymbol{k = 1, 2, \cdots}$ *until the active set* $\boldsymbol{\mathcal{A}^k}$ *does no longer change and* $\hat{\boldsymbol{R}}(\boldsymbol{U_h^k}) < \boldsymbol{TOL}\ \hat{\boldsymbol{R}}(\boldsymbol{U_0^k})$*:*

1. *Assemble the non-linear residual* $\boldsymbol{R}(\boldsymbol{U_h^k}) = -\boldsymbol{\nabla} \boldsymbol{E_\epsilon}(\boldsymbol{U_h^k})$.
2. *Compute active set* $\boldsymbol{\mathcal{A}^k} = \left\{ \boldsymbol{i} \mid (\boldsymbol{B^{-1}})_{\boldsymbol{ii}} (\boldsymbol{R}(\boldsymbol{U_h^k}))_{\boldsymbol{i}} + \boldsymbol{c}(\boldsymbol{\delta U_h^{k-1}})_{\boldsymbol{i}} > \boldsymbol{0} \right\}$.
3. *Assemble Jacobian matrix* $\boldsymbol{G} = \boldsymbol{\nabla^2} \boldsymbol{E_\epsilon}(\boldsymbol{U_h^k})$ *and right-hand-side* $\boldsymbol{F} = \boldsymbol{R}(\boldsymbol{U_h^k})$.
4. *Eliminate rows and columns in* $\boldsymbol{\mathcal{A}^k}$ *from* $\boldsymbol{G}$ *and* $\boldsymbol{F}$ *to obtain* $\hat{\boldsymbol{G}}$ *and* $\hat{\boldsymbol{F}}$.
5. *Solve linear system* $\hat{\boldsymbol{G}} \boldsymbol{\delta U_k} = \hat{\boldsymbol{F}}$.
6. *Find a step size* $\boldsymbol{0 < \omega \leq 1}$ *such that*

$$\boldsymbol{U_h^{k+1}} = \boldsymbol{U_h^k} + \boldsymbol{\omega} \boldsymbol{\delta U_h^k} \quad \textit{with}\ \hat{\boldsymbol{R}}(\boldsymbol{U_h^{k+1}}) < \hat{\boldsymbol{R}}(\boldsymbol{U_h^k}). \tag{57}$$

Remark 4.3. *In the stopping criterion in Algorithm 4.2, the residual on the inactive set* $\hat{\boldsymbol{R}}(\boldsymbol{U_h^k})$ *instead of full residual* $\boldsymbol{R}(\boldsymbol{U_h^k})$ *is used. The former is obtained by eliminating the constrained rows in the latter.*

4.3 Formulation of the Newton Residual and the Jacobian Matrix

From this subsection on, we now differ from [17] since the specific PDE (namely the residual and the Jacobian) is different. A monolithic scheme in which all equations are solved simultaneously is used to solve the aforementioned PDE system. However, the energy functional in Eq. (3) and its derived mixed-mode form are not convex with respect to both $\boldsymbol{u}$ and $\boldsymbol{\varphi}$, but convex with respect to only $\boldsymbol{u}$ or $\boldsymbol{\varphi}$ if the other is fixed. The critical term is the cross term $\left(\boldsymbol{(1-\kappa)\,\varphi^2 + \kappa} \right) \left(\boldsymbol{\sigma^+(u)}, \boldsymbol{e(u)} \right)$. In [17], the $\boldsymbol{\varphi}$ in the cross term is linearized by a time-lagging interpolation scheme $\boldsymbol{\varphi \approx \tilde{\varphi} := \tilde{\varphi}(\varphi^{n-1}, \varphi^{n-2})}$. A simple sub-iteration with a few cycles can be adopted in order to increase the accuracy comparable to fully-monolithic schemes [24].

However in this work, we choose a more conservative linearization scheme that $\boldsymbol{\varphi \approx \tilde{\varphi} := \varphi^{n-1}}$ to further increase the numerical robustness of the solver. Finally, the Newton residual (right-hand-side) is written as:

$$\begin{aligned}
\boldsymbol{F} \;=\; & \frac{\boldsymbol{1}}{\boldsymbol{2}} \left(\boldsymbol{(1-\kappa)\tilde{\varphi}^2 + \kappa} \right) \left(\left(\boldsymbol{\sigma_I^+(u) + \sigma_{II}^+(u), e(w)} \right) + \left(\boldsymbol{\sigma_I^+(w) + \sigma_{II}^+(w), e(u)} \right) \right) \\
& + \frac{\boldsymbol{1}}{\boldsymbol{2}} \left(\left(\boldsymbol{\sigma^-(u), e(w)} \right) + \left(\boldsymbol{\sigma^-(w), e(u)} \right) \right) \\
& + \boldsymbol{(1-\kappa)\,\varphi} \left(\left(\frac{\boldsymbol{\sigma_I^+(u)}}{\boldsymbol{G_{Ic}}} + \frac{\boldsymbol{\sigma_{II}^+(u)}}{\boldsymbol{G_{IIc}}} \right) \boldsymbol{:} \boldsymbol{e(u)}, \boldsymbol{\psi} \right) \\
& + \left(-\frac{\boldsymbol{1}}{\boldsymbol{\epsilon}} \boldsymbol{(1-\varphi, \psi)} + \boldsymbol{\epsilon} \left(\boldsymbol{\nabla \varphi, \nabla \psi} \right) \right)
\end{aligned} \tag{58}$$

and the corresponding Jacobian matrix is written as:

$$\begin{aligned} \boldsymbol{G} = & \frac{\mathbf{1}}{\mathbf{2}}\left((\mathbf{1}-\boldsymbol{\kappa})\tilde{\boldsymbol{\varphi}}^{\mathbf{2}}+\boldsymbol{\kappa}\right)\left(\left(\boldsymbol{\sigma}_{\boldsymbol{I}}^{+}(\boldsymbol{\delta u})+\boldsymbol{\sigma}_{\boldsymbol{II}}^{+}(\boldsymbol{\delta u}), \boldsymbol{e}(\boldsymbol{w})\right)+\left(\boldsymbol{\sigma}_{\boldsymbol{I}}^{+}(\boldsymbol{w})+\boldsymbol{\sigma}_{\boldsymbol{II}}^{+}(\boldsymbol{w}), \boldsymbol{e}(\boldsymbol{\delta u})\right)\right) \\ & +\frac{\mathbf{1}}{\mathbf{2}}\left(\left(\boldsymbol{\sigma}^{-}(\boldsymbol{\delta u}), \boldsymbol{e}(\boldsymbol{w})\right)+\left(\boldsymbol{\sigma}^{-}(\boldsymbol{w}), \boldsymbol{e}(\boldsymbol{\delta u})\right)\right) \\ & +(\mathbf{1}-\boldsymbol{\kappa})\,\boldsymbol{\varphi}\left(\left(\frac{\boldsymbol{\sigma}_{\boldsymbol{I}}^{+}(\boldsymbol{\delta u})}{\boldsymbol{G}_{\boldsymbol{Ic}}}+\frac{\boldsymbol{\sigma}_{\boldsymbol{II}}^{+}(\boldsymbol{\delta u})}{\boldsymbol{G}_{\boldsymbol{IIc}}}\right): \boldsymbol{e}(\boldsymbol{u})+\left(\frac{\boldsymbol{\sigma}_{\boldsymbol{I}}^{+}(\boldsymbol{u})}{\boldsymbol{G}_{\boldsymbol{Ic}}}+\frac{\boldsymbol{\sigma}_{\boldsymbol{II}}^{+}(\boldsymbol{u})}{\boldsymbol{G}_{\boldsymbol{IIc}}}\right): \boldsymbol{e}(\boldsymbol{\delta u}), \boldsymbol{\psi}\right) \\ & +\left(\frac{\mathbf{1}}{\boldsymbol{\epsilon}}(\boldsymbol{\delta\varphi}, \boldsymbol{\psi})+\boldsymbol{\epsilon}(\boldsymbol{\nabla\delta\varphi}, \boldsymbol{\nabla\psi})\right) \end{aligned} \tag{59}$$

4.4 Algorithm of the New Splitting Method

In this subsection we will introduce the algorithm of computing $\boldsymbol{\sigma}_{\boldsymbol{I}}^{+}(\boldsymbol{u})$, $\boldsymbol{\sigma}_{\boldsymbol{II}}^{+}(\boldsymbol{u})$ and $\boldsymbol{\sigma}^{-}(\boldsymbol{u})$ in Eq. (58), as well as $\boldsymbol{\sigma}_{\boldsymbol{I}}^{+}(\boldsymbol{\delta u})$, $\boldsymbol{\sigma}_{\boldsymbol{II}}^{+}(\boldsymbol{\delta u})$ and $\boldsymbol{\sigma}^{-}(\boldsymbol{\delta u})$ in Eq. (59). In finite-element implementation, $\boldsymbol{\delta u}$ is approximated using $\boldsymbol{\delta u_i v_i}$, where $\boldsymbol{\delta u_i}$ is the displacement increment on the nodal point, and $\boldsymbol{v_i}$ is the corresponding trial function. Therefore, what we need to compute for the Jacobian matrix is $\boldsymbol{\sigma}_{\boldsymbol{I}}^{+}(\boldsymbol{v})$, $\boldsymbol{\sigma}_{\boldsymbol{II}}^{+}(\boldsymbol{v})$ and $\boldsymbol{\sigma}^{-}(\boldsymbol{v})$ (Here we drop the subscript $\boldsymbol{i}$ to simplify the notation). The computation of $\boldsymbol{\sigma}_{\boldsymbol{I}}^{+}(\boldsymbol{w})$, $\boldsymbol{\sigma}_{\boldsymbol{II}}^{+}(\boldsymbol{w})$ and $\boldsymbol{\sigma}^{-}(\boldsymbol{w})$ is similar to that of $\boldsymbol{\sigma}_{\boldsymbol{I}}^{+}(\boldsymbol{v})$, $\boldsymbol{\sigma}_{\boldsymbol{II}}^{+}(\boldsymbol{v})$ and $\boldsymbol{\sigma}^{-}(\boldsymbol{v})$. The only difference is the input trial/test functions.

The algorithm to compute $\boldsymbol{\sigma}_{\boldsymbol{I}}^{+}(\boldsymbol{u})$, $\boldsymbol{\sigma}_{\boldsymbol{II}}^{+}(\boldsymbol{u})$ and $\boldsymbol{\sigma}^{-}(\boldsymbol{u})$ can be described as:

Algorithm 4.4. *On each quadrature point, at each Newton iteration step* $\boldsymbol{k = 1, 2, \ldots}$*, we have* $\boldsymbol{u := u^{k-1}}$*:*

1. *Compute the strain tensor* $\boldsymbol{e(u)}$*:*

$$\boldsymbol{e(u) = \frac{1}{2}(\nabla u + \nabla^{T} u).} \tag{60}$$

2. *Compute eigenvalues* $\boldsymbol{e_{p1}}$ *and* $\boldsymbol{e_{p2}}$ *(*$\boldsymbol{e_{p1} > e_{p2}}$*) and the matrix* $\boldsymbol{P}$ *consisting of normalized eigenvectors corresponding to* $\boldsymbol{e(u)}$*.*

3. *Compute the strain tensor under local crack coordinate* $\boldsymbol{e_c(u, \theta)}$ *with the input* $\boldsymbol{\theta = 0}$ *and* $\frac{\pi}{4}$*:*

$$\boldsymbol{e_c(u, \theta) = Q e_p Q^{T},} \tag{61}$$

where

$$\boldsymbol{e_p = \begin{pmatrix} e_{p1} & 0 \\ 0 & e_{p2} \end{pmatrix}} \tag{62}$$

$$\boldsymbol{Q = \begin{pmatrix} \cos(\theta) & \sin(\theta) \\ -\sin(\theta) & \cos(\theta) \end{pmatrix}.} \tag{63}$$

4. *Decompose* $\boldsymbol{e_c(u, \theta)}$ *into mode-I crack driving part* $\boldsymbol{e_{cI}^{+}(u, \theta)}$*, mode-II crack driving part* $\boldsymbol{e_{cII}^{+}(u, \theta)}$ *and non-dissipation part* $\boldsymbol{e_c^{-}(u, \theta)}$ *according to Eq.* (36)*, Eq.* (37) *and Eq.* (32)*.*

5. *Compute the counterparts of* $\boldsymbol{e_{cI}^{+}(u,\theta)}$, $\boldsymbol{e_{cII}^{+}(u,\theta)}$ *and* $\boldsymbol{e_{c}^{-}(u,\theta)}$ *in the global x-y coordinates:*

$$\begin{aligned} \boldsymbol{e_{I}^{+}(u,\theta)} &= \boldsymbol{B^{T}e_{cI}^{+}(u,\theta)B}, \\ \boldsymbol{e_{II}^{+}(u,\theta)} &= \boldsymbol{B^{T}e_{cII}^{+}(u,\theta)B}, \\ \boldsymbol{e^{-}(u,\theta)} &= \boldsymbol{B^{T}e_{c}^{-}(u,\theta)B}, \end{aligned} \tag{64}$$

where

$$\boldsymbol{B = QP^{T}.} \tag{65}$$

6. *Compute* $\boldsymbol{\sigma_{I}^{+}(u,\theta)}$, $\boldsymbol{\sigma_{II}^{+}(u,\theta)}$ *and* $\boldsymbol{\sigma^{-}(u,\theta)}$ *using Eq.* (29).

7. *Compute* $\boldsymbol{F(u,0)}$ *and* $\boldsymbol{F(u,\frac{\pi}{4})}$ *using Eq.* (40) *and determine the crack surface direction by:*

$$\boldsymbol{\theta_{n}} = \begin{cases} \mathbf{0} & \text{if } \boldsymbol{F(u,0) \geq F(u,\frac{\pi}{4})}, \\ \\ \dfrac{\boldsymbol{\pi}}{\mathbf{4}} & \text{if } \boldsymbol{F(u,0) < F(u,\frac{\pi}{4})}, \end{cases} \tag{66}$$

8. *Compute* $\boldsymbol{\sigma_{I}^{+}(u) := \sigma_{I}^{+}(u,\theta_{n})}$, $\boldsymbol{\sigma_{II}^{+}(u) := \sigma_{II}^{+}(u,\theta_{n})}$ *and* $\boldsymbol{\sigma^{-}(u) := \sigma^{-}(u,\theta_{n})}$ *using steps 3 - 6 with the input* $\boldsymbol{\theta = \theta_{n}}$.

The algorithm to compute $\boldsymbol{\sigma_{I}^{+}(v)}$, $\boldsymbol{\sigma_{II}^{+}(v)}$ and $\boldsymbol{\sigma^{-}(v)}$ is similar but more complex and can be described as:

Algorithm 4.5. *On each quadrature point, at each Newton iteration step* $\boldsymbol{k = 1, 2, \ldots}$, *we have* $\boldsymbol{u := u^{k-1}}$ *and* $\boldsymbol{v}$*:*

1. *Compute the strain tensor* $\boldsymbol{e(u)}$ *and the linearized strain tensor* $\boldsymbol{e(v)}$*:*

$$\boldsymbol{e(u)} = \frac{\mathbf{1}}{\mathbf{2}}\boldsymbol{(\nabla u + \nabla^{T} u)} \tag{67}$$

$$\boldsymbol{e(v)} = \frac{\mathbf{1}}{\mathbf{2}}\boldsymbol{(\nabla v + \nabla^{T} v)} \tag{68}$$

2. *Compute the linearized eigenvalues* $\boldsymbol{e_{p1}(v)}$ *and* $\boldsymbol{e_{p2}(v)}$ *and the matrix* $\boldsymbol{P(v)}$ *consisting of linearized normalized eigenvectors.*

3. *Compute the linearized strain tensor under local crack coordinate* $\boldsymbol{e_{c}(v)}$*:*

$$\boldsymbol{e_{c}(v) = Qe_{p}(v)Q^{T}}, \tag{69}$$

where

$$\boldsymbol{e_{p}(v)} = \begin{pmatrix} \boldsymbol{e_{p1}(v)} & \mathbf{0} \\ \mathbf{0} & \boldsymbol{e_{p2}(v)} \end{pmatrix} \tag{70}$$

$$\boldsymbol{Q} = \begin{pmatrix} \boldsymbol{\cos(\theta_{n})} & \boldsymbol{\sin(\theta_{n})} \\ \boldsymbol{-\sin(\theta_{n})} & \boldsymbol{\cos(\theta_{n})} \end{pmatrix} \tag{71}$$

4. *Decompose* $\boldsymbol{e_c(v)}$ *into mode-I crack driving part* $\boldsymbol{e_{cI}^+(v)}$*, mode-II crack driving part* $\boldsymbol{e_{cII}^+(v)}$ *and non-dissipation part* $\boldsymbol{e_c^-(v)}$ *by:*

$$\boldsymbol{e_{cI}^+(v)} = \begin{cases} \begin{pmatrix} \boldsymbol{e_{nn}(v)} & \boldsymbol{0} \\ \boldsymbol{0} & \boldsymbol{e_{ss}(v)} \end{pmatrix} & \text{if } \boldsymbol{e_{nn} + \frac{\lambda}{\lambda+2\mu} e_{ss} > 0} \text{ and } \boldsymbol{e_{ss} > 0}, \\ \begin{pmatrix} \boldsymbol{e_{nn}(v) + \frac{\lambda}{\lambda+2\mu} e_{ss}(v)} & \boldsymbol{0} \\ \boldsymbol{0} & \boldsymbol{0} \end{pmatrix} & \text{if } \boldsymbol{e_{nn} + \frac{\lambda}{\lambda+2\mu} e_{ss} > 0} \text{ and } \boldsymbol{e_{ss} \leq 0}, \\ \boldsymbol{0} & \text{if } \boldsymbol{e_{nn} + \frac{\lambda}{\lambda+2\mu} e_{ss} \leq 0}, \end{cases} \tag{72}$$

$$\boldsymbol{e_{cII}^+(v)} = \frac{\boldsymbol{1}}{\boldsymbol{2}} \begin{pmatrix} \boldsymbol{0} & \boldsymbol{e_{ns}(v)} \\ \boldsymbol{e_{sn}(v)} & \boldsymbol{0} \end{pmatrix}, \tag{73}$$

$$\boldsymbol{e_c^-(v)} = \boldsymbol{e_c(v) - e_{cI}^+(v) - e_{cII}^+(v)} \tag{74}$$

5. *Compute the counterparts of* $\boldsymbol{e_{cI}^+(v)}$*,* $\boldsymbol{e_{cII}^+(v)}$ *and* $\boldsymbol{e_c^-(v)}$ *in the global x-y coordinate:*

$$\begin{aligned} \boldsymbol{e_I^+(v)} &= \boldsymbol{(B(v))^T e_{cI}^+ B + B^T e_{cI}^+(v) B + B^T e_{cI}^+ B(v)}, \\ \boldsymbol{e_{II}^+(v)} &= \boldsymbol{(B(v))^T e_{cII}^+ B + B^T e_{cII}^+(v) B + B^T e_{cII}^+ B(v)}, \\ \boldsymbol{e^-(v)} &= \boldsymbol{(B(v))^T e^- B + B^T e^-(v) B + B^T e^- B(v)}, \end{aligned} \tag{75}$$

where

$$\boldsymbol{B(v) = Q\,(P(v))^T}. \tag{76}$$

6. *Compute* $\boldsymbol{\sigma_I^+(v)}$*,* $\boldsymbol{\sigma_{II}^+(v)}$ *and* $\boldsymbol{\sigma^-(v)}$ *using Eq.* (29)*.*

5 Numerical Tests

In this section we compare five existing energy splitting methods with our new splitting method. These six methods are named as Miehe's method [25], mixed-Miehe's method [32], Strobl's method [30, 29], Bryant's method [8], Freddi's method [14] and mixed-Freddi's method (our new method). It needs to be emphasized that:

- In the cases using Miehe's method and Freddi's method, the original phase-field model in Formulation 2.2 is used. While in the remaining cases, the mixed-mode phase-field model in Formulation 2.3 is used.
- In the cases using Strobl's method and Bryant's method, the crack directions are also computed using steps 1 - 7 in Algorithm 4.4 [2].

[2] Although in these two cases, $\frac{\partial \boldsymbol{F(u,\theta)}}{\partial \boldsymbol{\theta}}$ has different formulations from Eq. (40), the local maximum points of $\boldsymbol{F(u,\theta)}$ are still located at $\boldsymbol{\theta = 0}$ or $\boldsymbol{\theta = \frac{\pi}{4}}$ or both. Therefore, Algorithm 4.4 can still be used to compute crack surface direction in these two cases.

The comparison is based on three numerical tests, namely single-edge notched tension test, single-edge notched shear test and uniaxial compression test with an inclined notch. The first two tests are chosen for the following purposes:

- Showing the numerical robustness of our new splitting method.
- Showing that when the crack is pure mode-I, our new method coincides well with Freddi's method and does not overestimate force response.

The uniaxial compression test with an inclined notch is chosen to show that our new method can best capture the mixed-mode fracture geometry observed in the experiment. In each test, three uniformly-refined meshes are used to guarantee the reliability of the results. Two adaptively-refined meshes are also used to demonstrate the compatibility of our new method with adaptive mesh refinement.

5.1 Single-Edge Notched Tension Test

The configuration of this test is illustrated in Figure 2. We emphasize that the fracture generated under this configuration should be pure mode-I and the incorporation of $\boldsymbol{G_{IIc}}$, whatever value it has, should not change the crack propagation behavior. In the uniform mesh cases, the initial domain is five, six and seven times uniformly refined, leading to 4096, 16384 and 65536 mesh cells, and the minimum mesh size $\boldsymbol{h_{min} = 0.022mm, 0.011mm}$ and $\boldsymbol{0.0055mm}$ respectively. In the adaptive-refined mesh cases, the domain is first five times uniformly refined and then one and two times adaptively refined. The threshold for adaptive mesh refinement is set as $\boldsymbol{\varphi_{threshold} = 0.5}$.

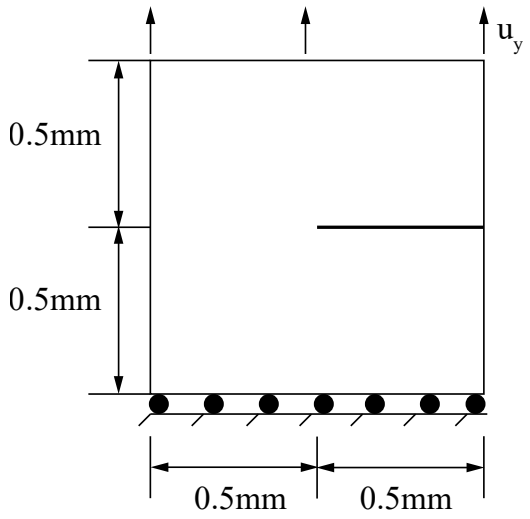

Figure 2: Configuration of single-edge notched tension test

For the displacements, a non-homogeneous time-dependent Dirichlet boundary condition is applied on the top boundary:

$$\boldsymbol{u_y(t) = \bar{u}t} \quad \text{with } \boldsymbol{\bar{u} = 1mm/s}, \tag{77}$$

where $\boldsymbol{t}$ denotes the total loading time. And the incremental time step size is set as $\boldsymbol{\Delta t = 1.0 \times 10^{-4} s}$. For the phase-field function, homogeneous Neumann boundary conditions are applied on the entire boundary.

We consider plane stress setting and use the mechanical parameters the same as those in [26], namely $\boldsymbol{\lambda = 121.15 kN/mm^2}$, $\boldsymbol{\mu = 80.77 kN/mm^2}$. In the cases using Miehe's method and Freddi's method, $\boldsymbol{G_c = 2.7 \times 10^{-3} kN/mm}$, otherwise $\boldsymbol{G_{Ic} = 2.7 \times 10^{-3} kN/mm}$ and $\boldsymbol{G_{IIc} = 10 G_{Ic}}$. Characteristic length $\boldsymbol{\epsilon = 2 h_{min}}$. Numerical parameter $\boldsymbol{\kappa = 1.0 \times 10^{-10}}$. Newton solver tolerance is set as $\boldsymbol{1.0 \times 10^{-6}}$.

Apart from crack geometry, we also check the average stress normal to the top boundary:

$$\boldsymbol{\sigma_y := \frac{\int_{\Gamma_{top}} n \cdot \sigma \cdot n dx}{\mathcal{H}(\Gamma_{top})}}, \tag{78}$$

where $\boldsymbol{\Gamma_{top} := \{(x, y) \in B \mid 0mm \leq x \leq 1mm, y = 1mm\}}$ is the top boundary, $\boldsymbol{n}$ is the outward unit vector normal to the top boundary surface and $\boldsymbol{\mathcal{H}}$ is the Hausdorff measure.

Figure 3 highlights the crack geometry of different splitting methods when the domain is seven times uniformly refined. It shows that:

- All methods except Bryant's can correctly capture the straight fracture path propagating from the center to the left boundary. The Newton's solver incorporating Bryant's method does not converge when the fracture initiates at the center, so the computation ends at $\boldsymbol{u = 6.3 \times 10^{-3} mm}$.

- The fracture propagation in mixed-Miehe's method is noticeably lagged compared with that in Miehe's method, although the fracture is pure Mode-I and the incorporation of $\boldsymbol{G_{IIc}}$ should not affect fracture propagation.

- The fracture propagation in mixed-Freddi's method is almost, if not exactly, the same as that in Freddi's method. Algorithm 4.4 identifies $\boldsymbol{\theta_n = 0}$ to be the direction of maximum dissipation, thus $\boldsymbol{\sigma_{II}^+ = 0}$ and the incorporation of $\boldsymbol{G_{IIc}}$ does not affect the fracture propagation.

Figure 4 displays the Newton iteration numbers for different splitting methods when the domain is seven times uniformly refined. It shows that:

- The Newton solvers incorporating Bryant's, Strobl's and Freddi's methods have worse performance than those incorporating other methods. In Bryant's case, the Newton solver stagnates at the $\boldsymbol{63^{th}}$ time step. In Strobl's case, the Newton iteration number fluctuates between the $\boldsymbol{80^{th}}$ and $\boldsymbol{110^{th}}$ time steps, with the highest Newton iteration number **134**. In Freddi's case, the Newton iteration number increases to **35** after the $\boldsymbol{63^{th}}$ time step and remains at high level until the crack reaches the boundary at the $\boldsymbol{114^{th}}$ time step.

- The Newton solver incorporating mixed-Freddi's method has better performance than that incorporating Freddi's method. Between the $\boldsymbol{63^{th}}$ and $\boldsymbol{114^{th}}$ time steps mixed-Freddi's case has comparable Newton step numbers with Miehe's case. While Freddi's case has Newton step number two times more than that in Miehe's case.

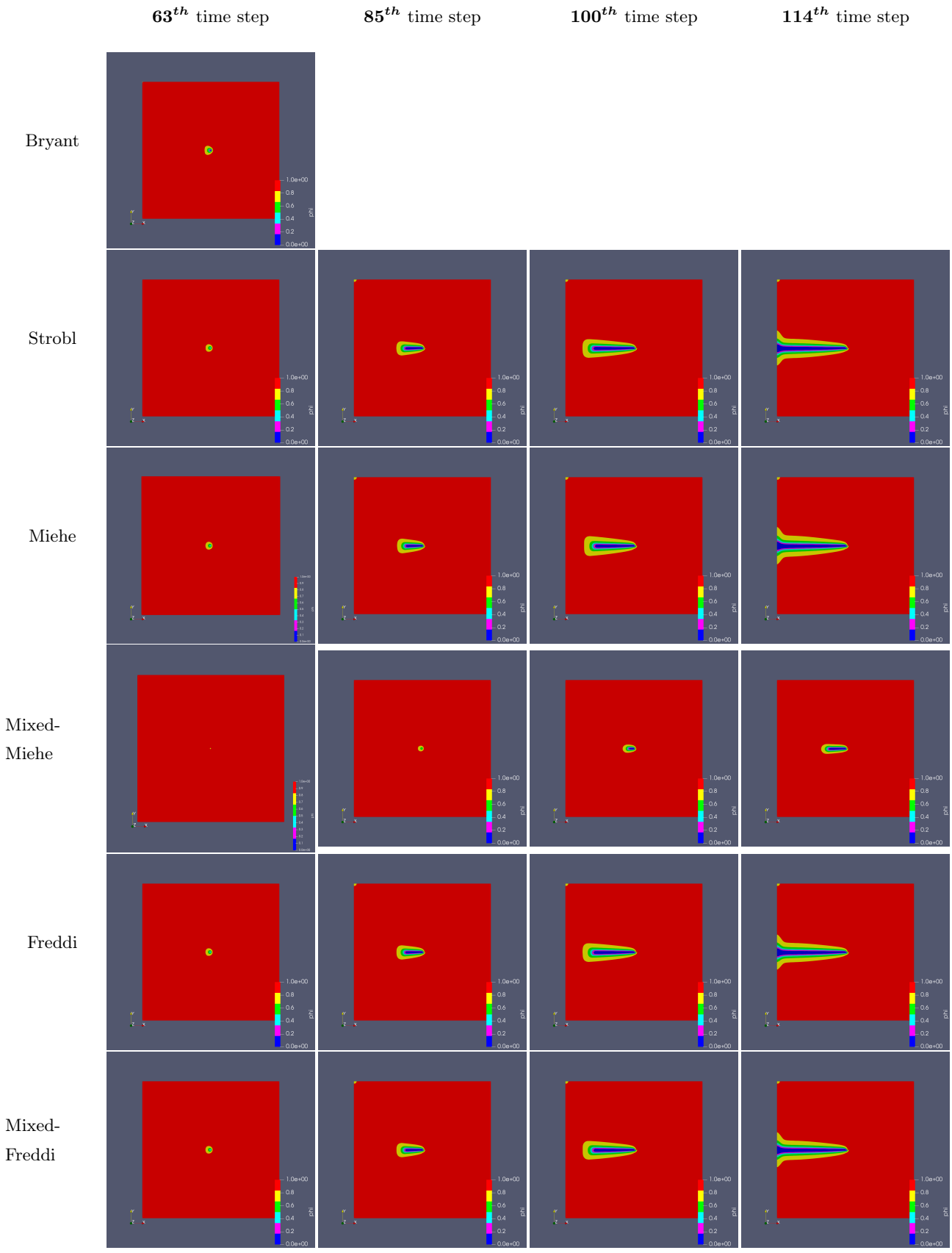

Figure 3: Crack geometries of different splitting methods in single-edge notched tension test

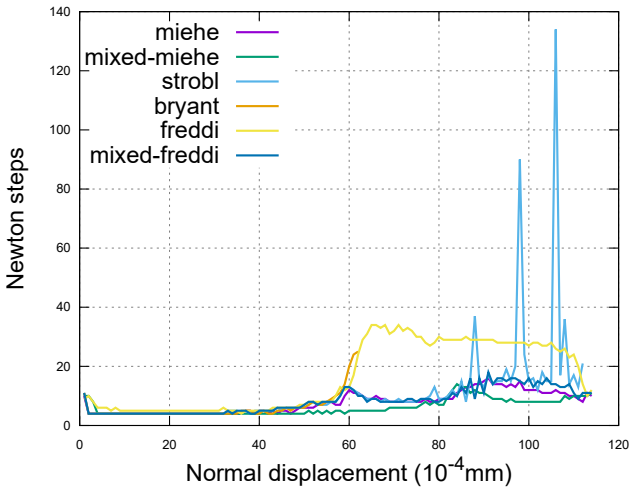

Figure 4: Newton iteration numbers of different splitting methods under seven global refinement in single-edge notched tension test

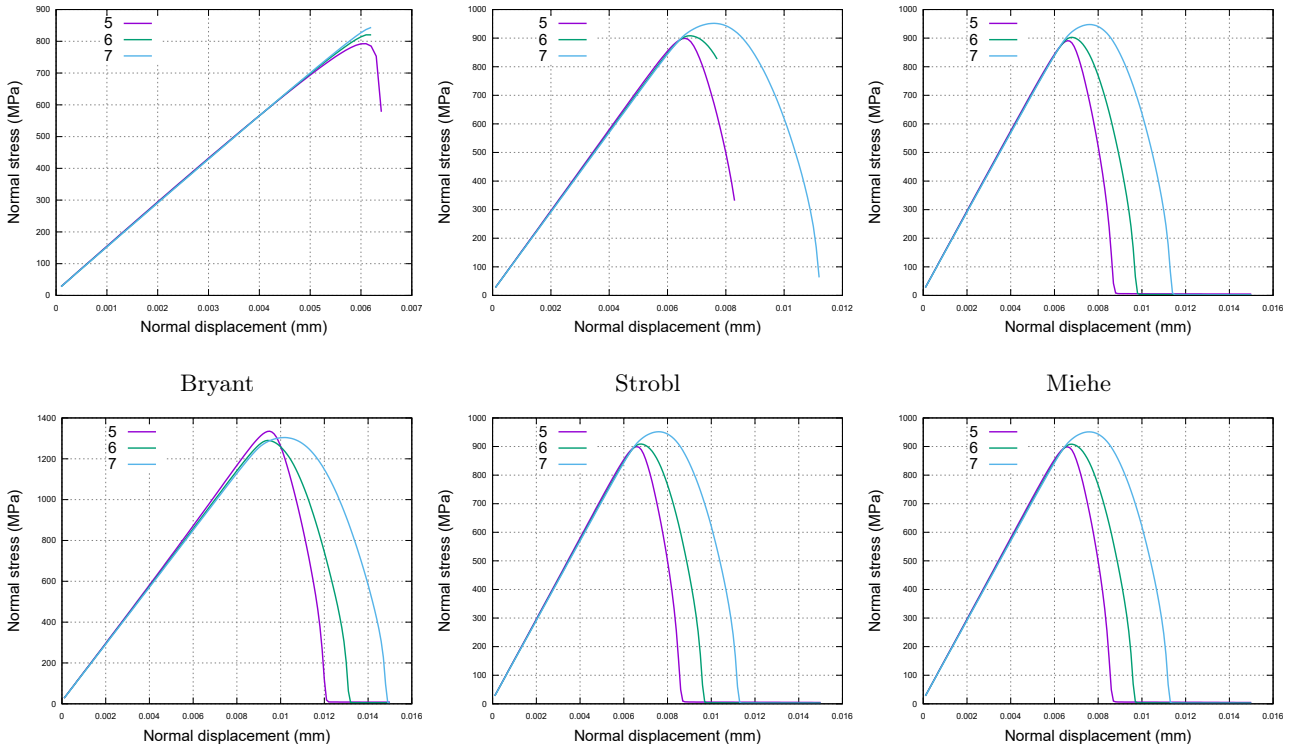

Figure 5: Load-displacement curves of different splitting methods under three uniformly-refined meshes for single-edge notched tension test

Figure 5 displays the load-displacement curves of the six splitting methods under three uniformly-refined meshes. It shows that:

- All but Bryant's and Strobl's methods can capture the full loading and unloading processes. In Bryant's and Strobl's cases, the Newton solver stagnates before the load decreases to zero.
- In all but mixed-Miehe's cases, the load-displacement curves of the same splitting method are

consistent under three different meshes. But the maximum load response increases as mesh refinement increases and ϵ decreases. This phenomenon has also been observed in [33]. However in mixed-Miehe's case, the finest mesh, seven times global refinement, has the intermediate load response, indicating the instability of the method.

In Figure 6, we observe the load-displacement curves of the six splitting methods when the domain is seven times refined. It shows that:

- All but Bryant's and mixed-Miehe's methods have almost the same load-displacement curves. Particularly, the load-displacement curves of Strobl's, Freddi's and mixed-Freddi's are almost identical that they overlap with each other. The only difference among them is that the curve terminated earlier in Strobl's case, which can also be observed in Figure 5.

- In Bryant's case, the load-displacement curve terminates early due to the Newton solver non-convergence. In mixed-Miehe's case, the maximum load response is about 37% higher than that in other cases. This phenomenon verifies the overestimation problem of mixed-Miehe's method, as mentioned in Section 3.

We remark that although Bryant's method worked well in uniaxial compression tests with single and multiple notches in [8], it appeared to be not numerically-robust in all of our tests; namely the single-edge notched tension, single-edge notched shear and uniaxial compression with an inclined notch. But Bryant's model is still a significant reference for this paper as it gives inspiration for how to determine the crack surface direction.

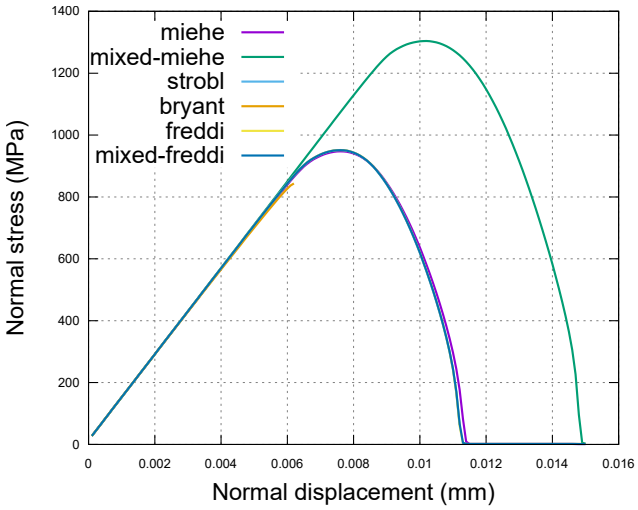

Figure 6: Load-displacement curves of different splitting methods under seven global refinement in single-edge notched tension test

Figure 7 shows the crack geometry of mixed-Freddi's splitting method under five times global refinement plus two adaptive refinement cycles (5+2). Comparing Figure 7 with the last row in Figure 3, we observe that the crack in 5+2 refinement case has almost the same propagation progress and smeared width as those in 7+0 refinement case.

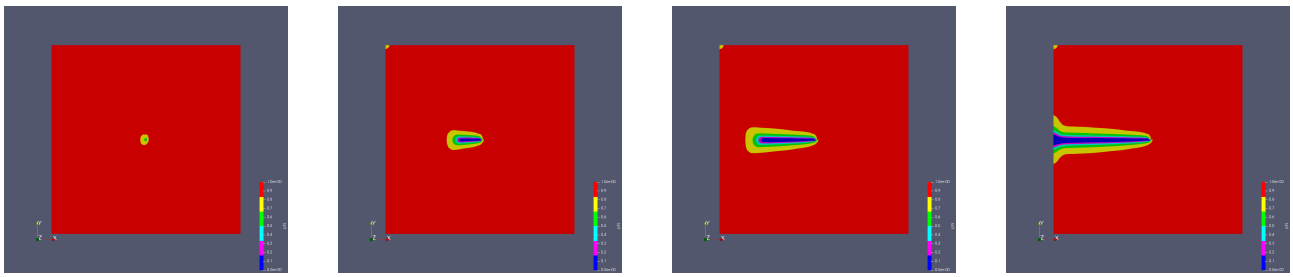

$\mathbf{63}^{th}$ time step $\mathbf{85}^{th}$ time step $\mathbf{100}^{th}$ time step $\mathbf{114}^{th}$ time step

Figure 7: Crack geometries of mixed-Freddi's splitting method under 5+2 mesh refinement in single-edge notched tension test

In Figure 8 the load-displacement curves of mixed-Freddi's method under 5+0, 5+1 and 5+2 refinement are displayed. Comparing Figure 8 with the last sub-figure in Figure 5, we can see that the 5+1 and 5+2 refined cases have very similar load responses with the 6+0 and 7+0 refined cases.

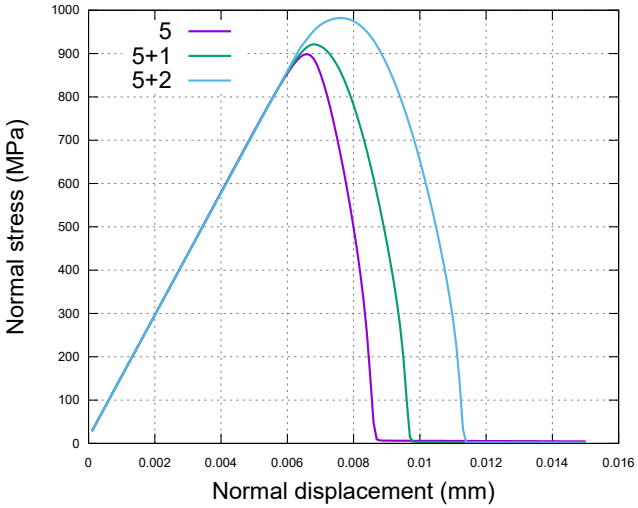

Figure 8: Load-displacement curves of mixed-Freddi's method under 5+0, 5+1 and 5+2 refinement in single-edge notched tension test.

In conclusion of this first numerical example, mixed-Freddi's method works well with adaptive mesh refinement. Here, almost the same crack geometry and load response of uniform refinement case can be captured, but with much less degrees of freedom (DoFs). For example, the 7+0 case has 198531 DoFs through the entire computation process, while the 5+2 case has only 12771 DoFs at the $\mathbf{1}^{st}$ time step and 18903 DoFs at the $\mathbf{114}^{th}$ time step. Illustration of meshes for the 7+0 case (only uniformly refined) and 5+2 case (five times uniformly refined and two times adaptively refined) for the single-edge notched tension test are displayed in Figure 9.

5.2 Single-Edge Notched Shear Test

The configuration of this test is illustrated in Figure 10. This test is widely used to check whether an energy splitting method is capable of only inducing fractures in the tensile-loaded region. If the splitting method fails to replicate this behavior or if no splitting method is used, we will get an incorrect branched crack geometry, as shown in for instance already in very early studies [7]. We emphasize that

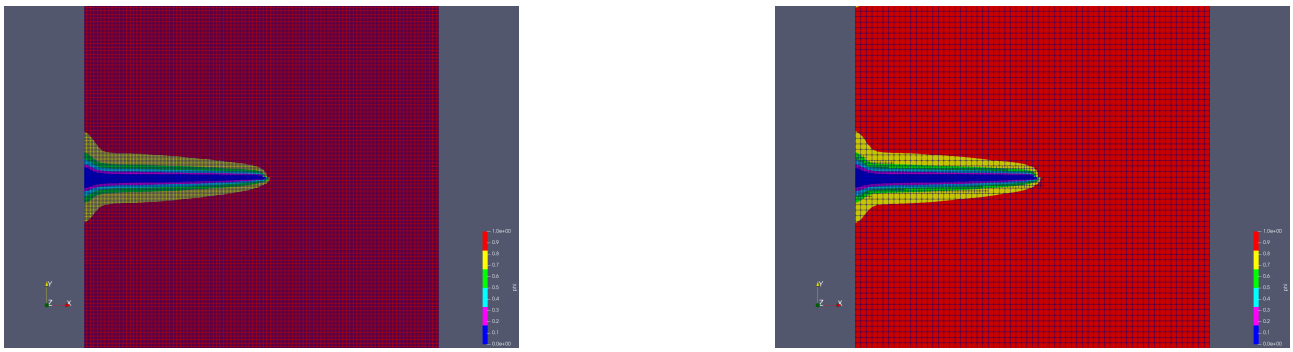

7+0 case 5+2 case

Figure 9: Mesh comparison between 7+0 and 5+2 cases using mixed-Freddi's method for single-edge notched tension test

the fracture generated under this configuration is also pure mode-I although shear load is applied at the top boundary. The maximum principal stress in the tensile-loaded region drives the crack to propagate [8].

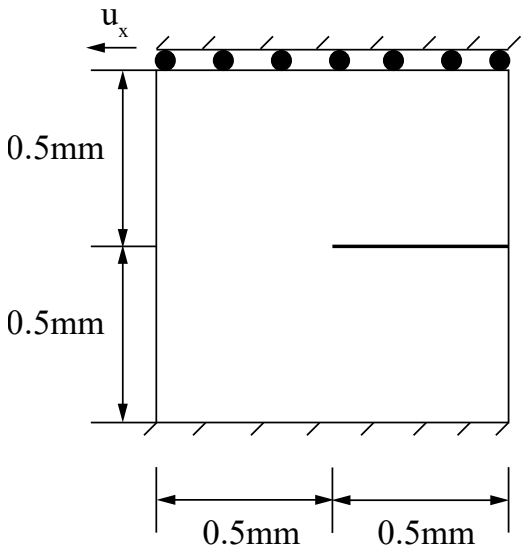

Figure 10: Configuration of single-edge notched shear test

The mesh refinement strategy, mechanical and numerical parameters are the same as those in the single-edge notched tension test presented in the previous subsection.

The boundary condition is similar to that in the tension case, but the loading direction is now tangential to the top boundary:

$$\boldsymbol{u_x(t) = \bar{u}t} \quad \text{with } \boldsymbol{\bar{u} = 1mm/s}, \tag{79}$$

Correspondingly, we now check the average stress tangential to the top boundary:

$$\boldsymbol{\sigma_x := \frac{\int_{\Gamma_{top}} s \cdot \sigma \cdot n dx}{\mathcal{H}(\Gamma_{top})}}, \tag{80}$$

where $\boldsymbol{s}$ is the unit vector tangential to the top boundary surface.

Figure 11 displays the crack geometry of different splitting methods when the domain is seven times uniformly refined. It shows that:

- All methods except Bryant's can correctly capture the curved fracture path propagating from the center to the lower-left corner. The Newton's solver incorporating Bryant's method does not converge when the fracture initiates at the center so the computation ends at $\boldsymbol{u = 8.9 \times 10^{-3} mm}$.

- The fracture propagation in mixed-Miehe's case is noticeably lagged compared with that in Miehe's case. While the fracture propagation in mixed-Freddi's case is almost, if not exactly, the same as that in Freddi's case.

In Figure 12 the Newton iterations are monitored for different splitting methods when the domain is seven times uniformly refined. The Newton solver performances of different splitting methods are similar to those in the tension case. In detail:

- The Newton solvers incorporating Bryant's, Strobl's and Freddi's methods still have much higher iteration numbers at certain time steps than those incorporating other splitting methods.

- The Newton solver incorporating mixed-Freddi's method has approximately 10 Newton iteration steps at each time step when the crack is propagating, showing a better performance than the solver incorporating Freddi's method.

Figure 13 shows the load-displacement curves of the six splitting methods under three uniformly-refined meshes. Again, the findings are similar to those in single-edge notched tension test. In detail:

- All but Bryant's and Strobl's methods can capture the full loading-unloading process.

- In all cases, the maximum load response increases as mesh refinement increases and $\boldsymbol{\epsilon}$ decreases.

- After the crack reaches the boundary, the tangential load, instead of going to zero, starts to increase. According to [1], this nonphysical phenomenon is caused by the elastic response of the cracked specimen clamped at the undamaged lower right portion of the boundary.

We remark that if Amor's method [4] and Bryant's method [8] are used, the stresses can go completely to zero in the single-edge notched shear test when the crack reaches the boundary (see for instance [1]). However in our shear tests: (1) Amor's method results in an undesirable sub-horizontal crack geometry; (2) Bryant's method is not numerically-robust and only works in very limited cases.

Figure 14 displays the load-displacement curves of the six splitting methods when the domain is seven times refined. We observe:

- All but Bryant's and mixed-Miehe's methods have similar load-displacement curves. Specifically, the load-displacement curve of mixed-Freddi's method overlaps with that of Strobl's method, and it only diverges from that of Freddi's method after the crack reaches boundary and load starts to re-increase.

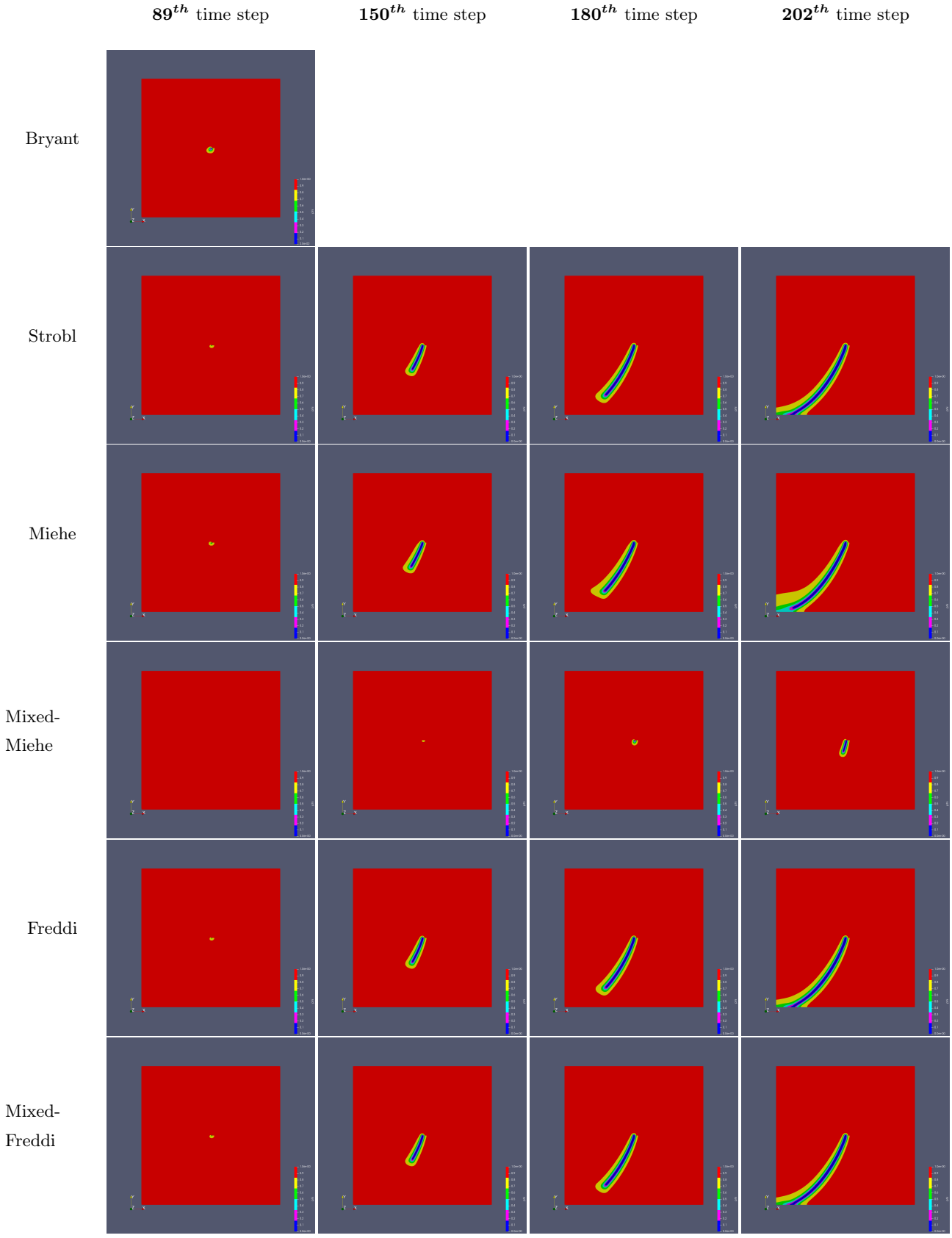

Figure 11: Crack geometries of different splitting methods for the single-edge notched shear test

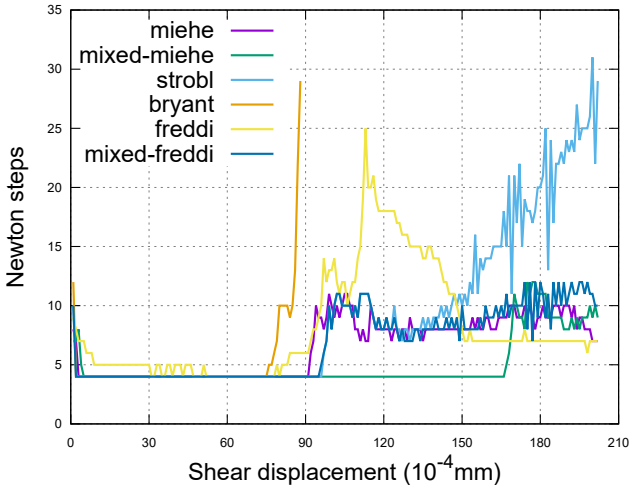

Figure 12: Newton iterations of different splitting methods under seven global refinement for the single-edge notched shear test

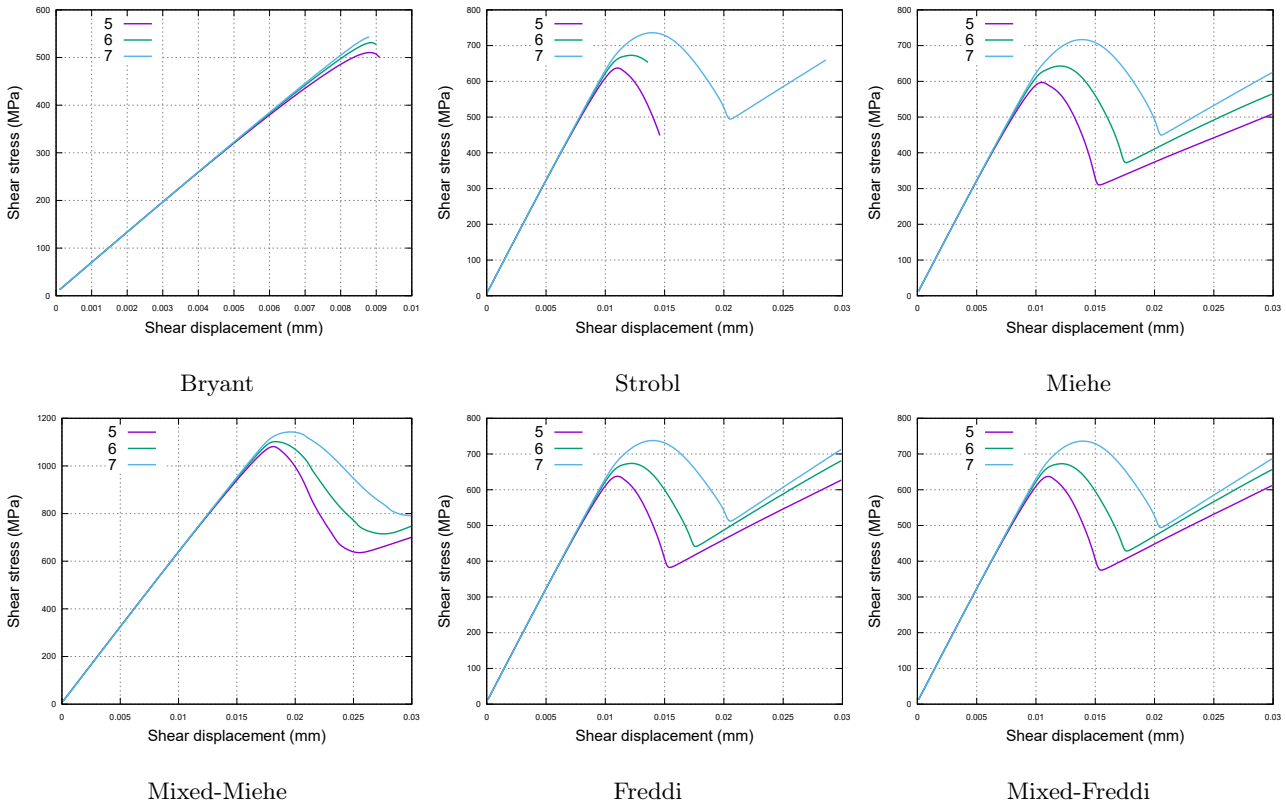

Figure 13: Load-displacement curves of different splitting methods under three uniformly-refined meshes in single-edge notched shear test

- In Bryant's case, the load-displacement curve terminates early due to the Newton solver non-convergence. In mixed-Miehe's case, the maximum load response is about 59% higher than that in other cases.

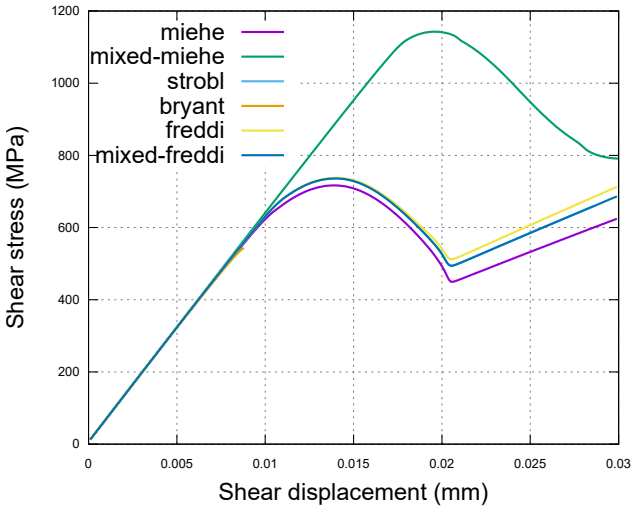

Figure 14: Load-displacement curves of different splitting methods under seven global refinement in single-edge notched shear test

Similar to the single-edge notched tension test, Figure 15 and Figure 16 show that employing adaptive mesh refinement reproduces the findings obtained with uniform refinement, but with much less DoFs. Illustration of meshes for the 7+0 case (only uniformly refined) and 5+2 case (five times uniformly refined and two times adaptively refined) for the single-edge notched shear test are displayed in Figure 17.

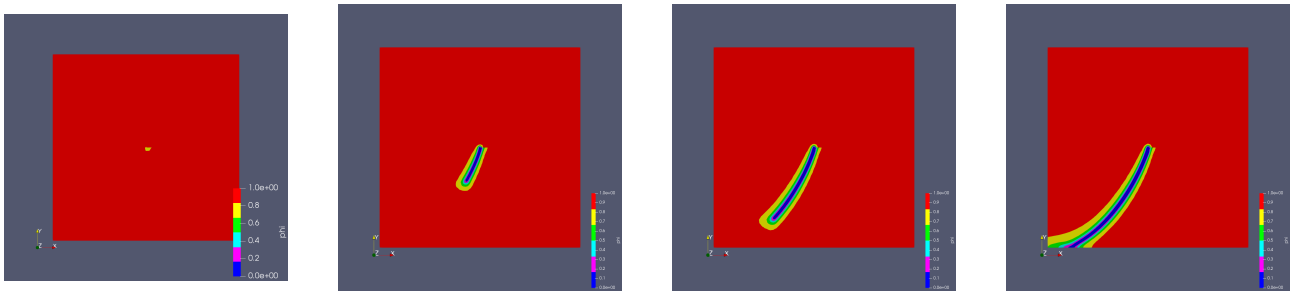

89th time step **150**th time step **180**th time step **202**th time step

Figure 15: Crack geometries of mixed-Freddi's splitting method under 5+2 mesh refinement in single-edge notched shear test

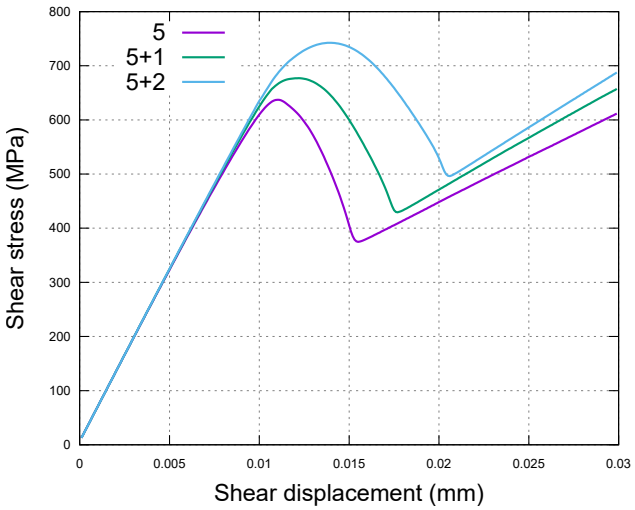

Figure 16: Load-displacement curves of mixed-Freddi's method under 5+0, 5+1 and 5+2 refinement in single-edge notched shear test.

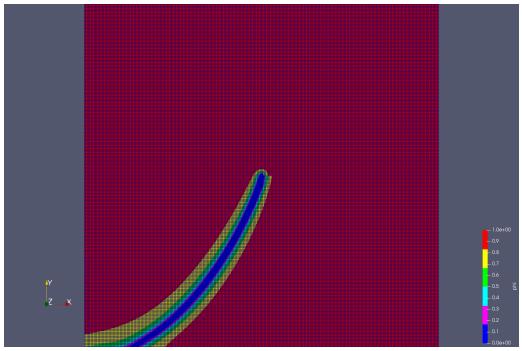

7+0 case

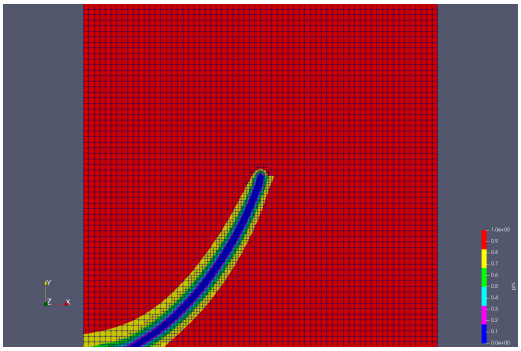

5+2 case

Figure 17: Mesh comparison between 7+0 and 5+2 cases using mixed-Freddi's method for single-edge notched shear test

5.3 Uniaxial Compression Test with an Inclined Notch

The uniaxial compression test with an inclined notch is chosen to demonstrate the capabilities of the different energy splitting methods in capturing mixed mode-I and mode-II fracture geometries. Since Bryant's and Strobl's methods have been proven to be numerically non-robust in the previous tests, we only present and compare Miehe's, mixed-Miehe's, Freddi's and mixed-Freddi's methods in this test. As it is already reviewed in [31], various experiments have been done to study the crack geometry in specimens containing a single flaw under uniaxial compression. To choose one experiment from them as the benchmark for our numerical test, we make the following considerations:

- We want to find an experimental setting which is featured with distinct mode-I and mode-II fractures.
- Since we only consider two-dimensional situations in the present study, we want to find an experimental configuration satisfying the plane stress setting. More specifically, the dimension of the specimen in the $\boldsymbol{z}$ direction should be much smaller than the dimensions in the $\boldsymbol{x}$ and $\boldsymbol{y}$ directions. And the crack should penetrate through the specimen in the $\boldsymbol{z}$ direction.
- Since we do not consider the friction force on the fracture surface, we want to find an configuration with an open flaw, i.e. a notch, so that this frictionless simplification has minor influence on the comparison between simulation and experiment results.

A first possibility is the limestone experimental setting presented in [22] which is chosen as numerical test case in [32]. However, in this setting, the primary and secondary cracks are all mode-I cracks [22, 21]. Instead, we choose the marble experimental setting in [20], in which distinct mode-I and mode-II fractures are induced. As shown in Figure 18, the crack geometry of this setting can be summarized as:

- Mode-I cracks: 1 - primary forward tensile cracks (PFTCs), 2 - secondary forward tensile cracks (SFTCs) and 3 - backward tensile cracks (BTCs).
- Mode-II cracks: 4 - forward shear belts (FSBs) and 5 - backward shear belts (BSBs).

According to [20], the formation of FSBs and BSBs is caused by the coalescence of micro-cracks. These micro-cracks are essential to increasing the production rates in the oil and gas industry as they can largely increase the permeability of rocks (see for instance [34]).

The configuration of this test is illustrated in Figure 19. The uniformly-refined base mesh is first generated with 7952 mesh cells. On this basis: (1) In the uniformly-refined mesh cases, the domain is zero, one and two times uniformly refined, leading to 7952, 31808 and 127232 mesh cells, and the minimum mesh size $\boldsymbol{h_{min} = 1.17mm, 0.59mm}$ and $\boldsymbol{0.29mm}$ respectively. (2) In the adaptively-refined mesh cases, the domain is further one and two times adaptively refined. The threshold for adaptive mesh refinement is set as $\boldsymbol{\varphi_{threshold} = 0.5}$.

For the displacements, a compressive Dirichlet boundary condition is applied at the top boundary:

$$\boldsymbol{u_y(t) = \bar{u}t} \quad \text{with } \boldsymbol{\bar{u} = -1mm/s.} \tag{81}$$

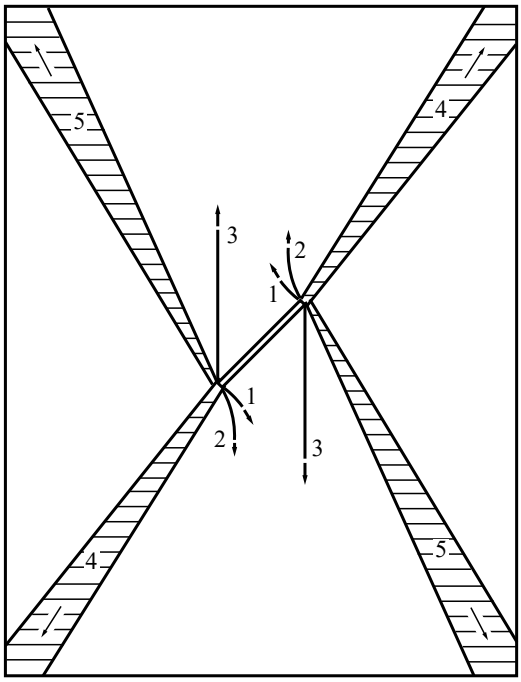

Figure 18: Experimental crack geometry of marble in uniaxial compression test with an inclined notch [20]

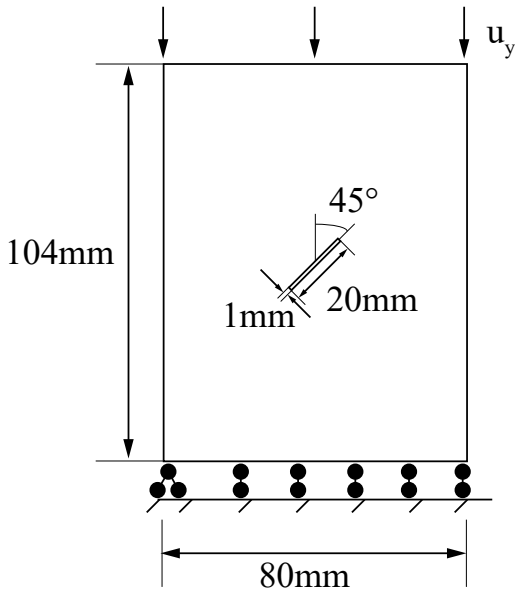

Figure 19: Configuration of uniaxial compression test with an inclined notch.

And the incremental time step size is set as $\boldsymbol{\Delta t = 1.0 \times 10^{-3} s}$. For the phase-field function, homogeneous Neumann boundary conditions are applied on the entire boundary.

We consider plane stress setting and use the mechanical parameters as following: Young's modulus $\boldsymbol{E = 63.5 kN/mm^2}$ [20], Poisson's ratio $\boldsymbol{\nu = 0.21}$. In the cases using Miehe's method and Freddi's method, $\boldsymbol{G_c = 11.0 \times 10^{-6} kN/mm}$, otherwise $\boldsymbol{G_{Ic} = 11.0 \times 10^{-6} kN/mm}$ and $\boldsymbol{G_{IIc} = 10 G_{Ic}}$ [32]. The parameters $\boldsymbol{\epsilon}$, $\boldsymbol{\kappa}$ and the Newton solver tolerance are set to the same values as in the previous two tests.

Apart from the crack geometry, we also check the average compressive stress normal to the top boundary:

$$\boldsymbol{\sigma_y := -\frac{\int_{\Gamma_{top}} n \cdot \sigma \cdot n dx}{\mathcal{H}(\Gamma_{top})}}. \tag{82}$$

In this test, the zero and one time uniformly-refined cases have similar crack propagation behaviors. But the two times uniformly-refined case behaves differently. Therefore, we present the crack geometries of both one and two times uniformly-refined cases.

In Figure 20 the crack geometries of different splitting methods are shown when the domain is one time uniformly refined. In this test, the crack propagation progresses (i.e., the paths and lengths) of different splitting methods vary significantly. Therefore, for different splitting methods we present our findings at different time steps. It can be observed that:

- Stage(a): In all four cases, PFTCs initiate near the notch tip and propagate in the direction sub-perpendicular to the notch surface.

- Stage(b): In Freddi's case, PFTCs propagate in a curvature manner and gradually turn to the direction parallel with the loading direction. In mixed-Freddi's case, PFTCs propagate in the same manner as that in Freddi's case. Additionally, the FSBs and BSBs start to form. In Miehe's and mixed-Miehe's cases, PFTCs become fat at the early propagation stage and has a tendency to propagate towards the upper-right and lower-left corners. And BTCs initiate sub-perpendicular to the notch surface. In the mean time, FSBs and BSBs start to form.

- Stage(c): In Freddi's case, the PFTCs continue propagating in the vertical direction and BTCs start to initiate. In mixed-Freddi's case, the PFTCs and BTCs propagate in the same manner as that in Freddi's case. FSBs and BSBs become larger and the phase-field variable in them become lower, indicating further damage. In Miehe's case, the PFTCs propagate towards the corners, BTCs propagate sub-vertically, and the FSBs and BSBs become layered. In the meantime, there are two cracks initiating near the upper-right and lower-left corners. In mixed-Miehe's case, the crack propagation behavior is very similar to that in Miehe's case, except that the PFTCs now propagate sub-vertically instead of towards the corners.

- Stage(d): In Freddi's case, the PFTCs reach the boundary and BTCs propagate vertically to some extent. In mixed-Freddi's case, the PFTCs and BTCs propagate in a similar manner as those in Freddi's case. And the FSBs and BSBs continue evolving into the final X-shape. In Miehe's case, the PFTCs and the cracks initiating near the corners propagate towards each other and finally

get connected. In mixed-Miehe's case, the cracks initiating near the corners propagate towards and get connected to the middle parts of PFTCs, finally forming a branched crack geometry.

It is clear that Miehe's and mixed-Miehe's methods cannot capture the correct crack geometry in this test. They lead to an 'average damage' state in the uniaxially compressed specimen. Freddi's method can only capture the PFTCs geometry. Mixed-Freddi's splitting method can best capture both the mode-I and mode-II crack characteristics. The only discrepancy is that there are no SFTCs. This discrepancy is acceptable because in the experiment SFTCs propagate in a very similar manner as PFTCs, and the initiation positions of SFTCs and PFTCs are very near to each other.

Figure 21 displays the crack geometries when the domain is two times uniformly refined. The main differences between Figure 21 and Figure 20 can be summarized as follows:

- In Miehe's and mixed-Miehe's cases, the PFTCs start branching at stage(b). Thus the crack geometries in these two cases become more similar to each other.

- In Freddi's and mixed-Freddi's cases, PFTCs stop propagating after having reached certain lengths. The load response continue increasing until the solver dies. The specimen does not rupture at the end of the simulation.

The reason for crack branching in Miehe's and mixed-Miehe's cases might be that the cracks become thinner as $\boldsymbol{\epsilon}$ decreases, so the originally merged neighboring cracks now become distinct from each other and thus exhibiting the branching behavior. The reason for the non-rupture phenomenon in Freddi's and mixed-Freddi's cases is more complicated. One physical interpretation is that the crack smeared width $\boldsymbol{\epsilon}$ can represent the width of micro-crack zones surrounding the propagating macro-cracks. In rocks, there are usually wide micro-crack zones around macro cracks [11]. But in more isotropic and homogeneous materials like poly(methyl methacrylate) (PMMA), the macro cracks are sharper and there are very thin or even no micro-crack zones [6]. In other words, when other parameters are fixed, large $\boldsymbol{\epsilon}$ can better describe the cracking behavior of rocks while small $\boldsymbol{\epsilon}$ is more suitable for PMMA. Therefore, in the one time refined case, the simulated crack geometries are similar to those in the marble experiment, where the specimen ruptures as cracks propagate to the boundary. While in the two times refined case, the simulated crack geometries are similar to those in the PMMA experiment, as mentioned in [21, 22, 23], where PFTCs stop propagating after having reached certain length and specimen does not rupture even when load increases to a very high level. We also want to emphasize that in this extreme case, the mixed-Freddi's method is numerically more robust than Freddi's method, as the PFTCs can propagate further in mixed-Freddi's case.

Figure 22 monitors the load-displacement curves of the four splitting methods under three times uniformly refined meshes. We observe:

- As it is already stated in Eq. (5), we use a linear elastic constitutive law in the phase-field model. However, in Miehe's and mixed-Miehe's cases, the load-displacement curves exhibit softening behavior before peak loading, which might be caused by the wide-smeared crack profile. In Freddi and mixed-Freddi's cases, the load-displacement curves are straight lines from zero loading to peak loading, which is a typical behavior of linear-elastic brittle material. Therefore, we can

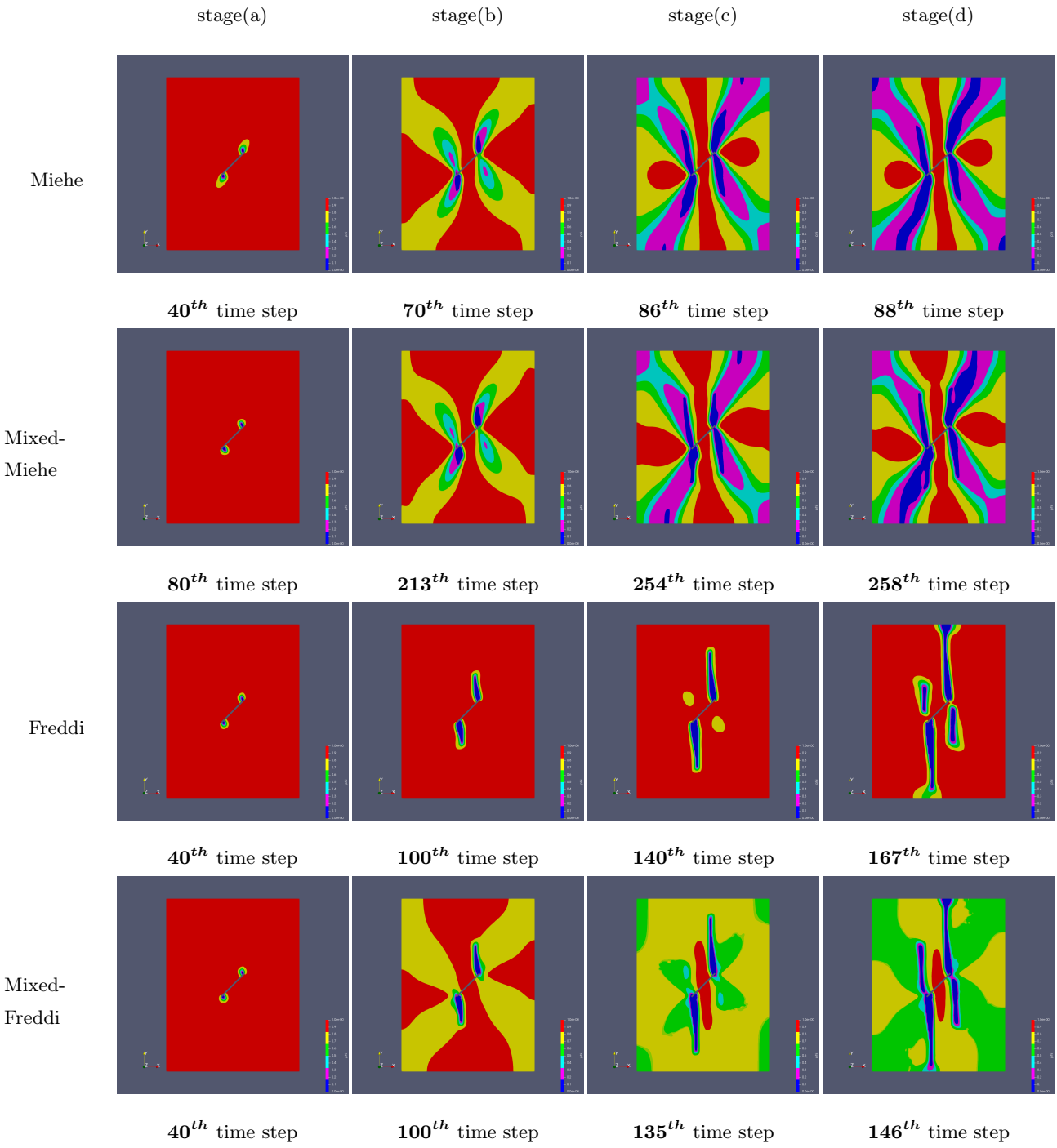

Figure 20: Crack geometries of different splitting methods when the domain is one time uniformly refined in the uniaxial compression test with an inclined notch

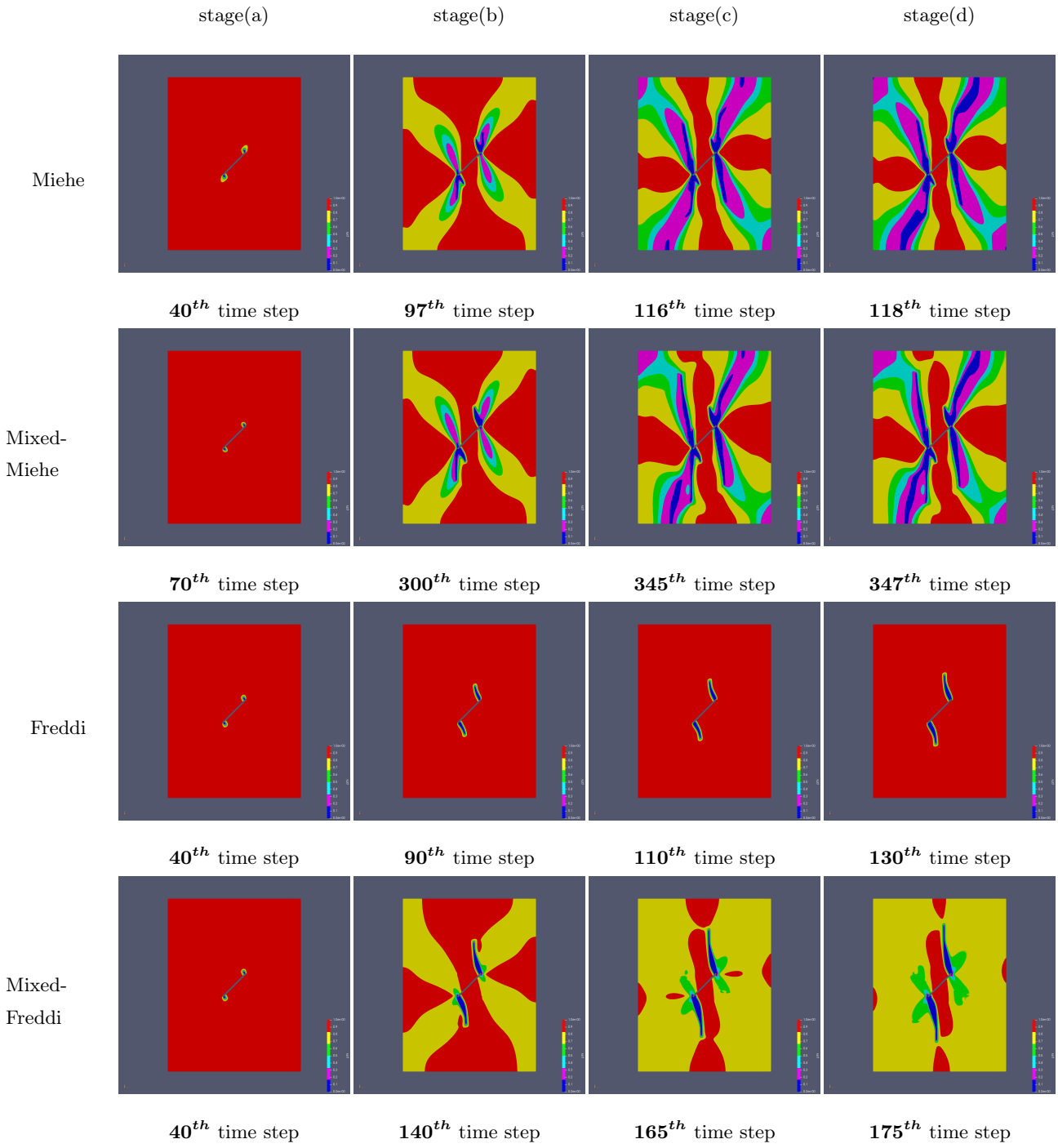

Figure 21: Crack geometries of different splitting methods when the domain is two times uniformly refined in uniaxial compression test with an inclined notch

conclude that Freddi's and mixed-Freddi's method can better capture the constitutive behavior in this test.

- When the domain is zero and one time uniformly refined, The simulation continues until the load starts to decrease (when cracks reach boundaries) in all four cases. When the domain is two times uniformly refined, the simulation still continues until the load starts to decrease in Miehe's and mixed-Miehe's cases. While in Freddi's and mixed-Freddi's cases, the simulation ends before the load decreases. Again we can see that mixed-Freddi's method is numerically more robust than Freddi's method, as the load-displacement curve extends further in mixed-Freddi's case.

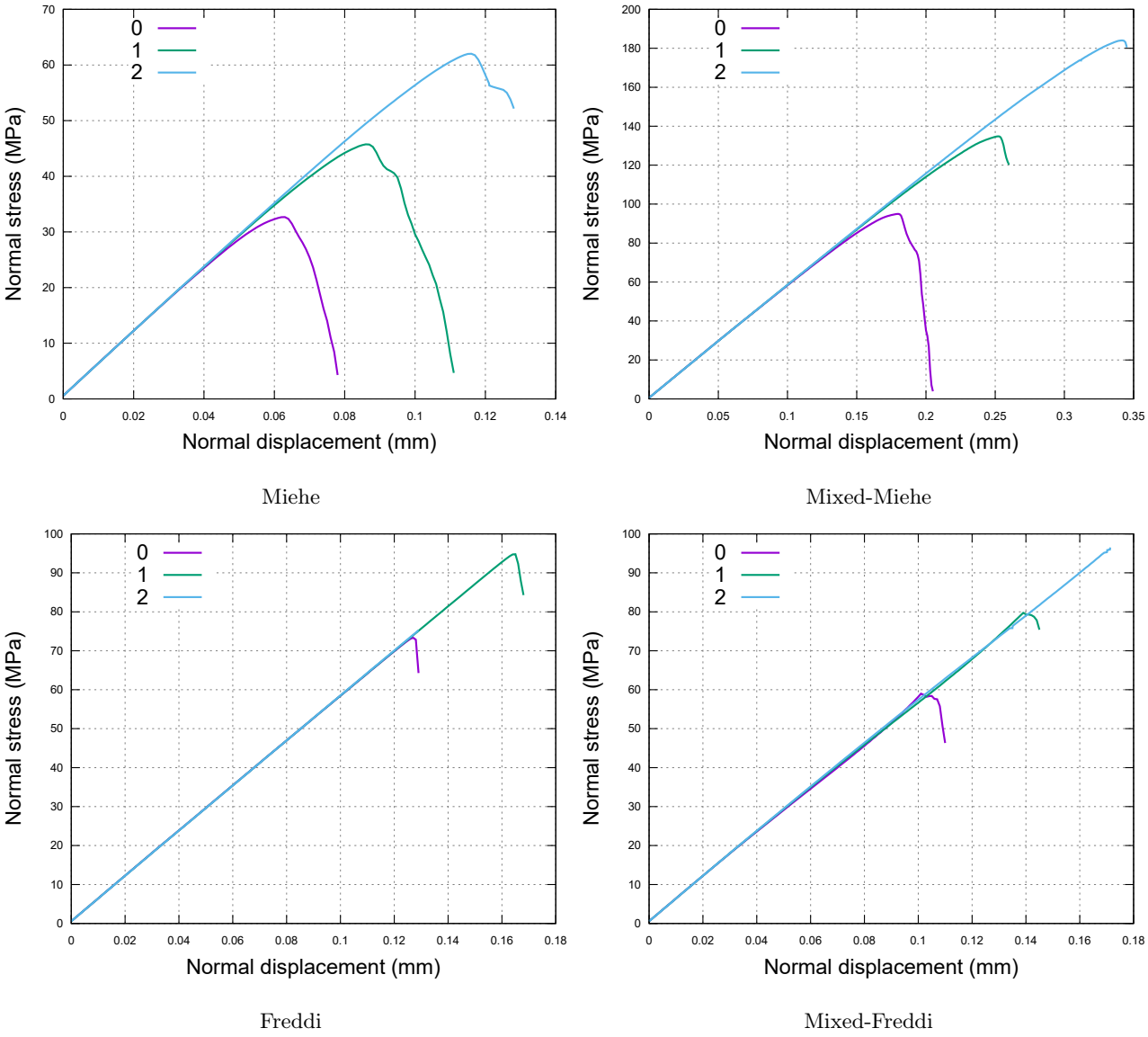

Figure 22: Load-displacement curves of different splitting methods under three uniformly-refined meshes in uniaxial compression test with an inclined notch

As before, Figure 23 and Figure 24 show that tests using adaptive refinement can reproduce the results in tests using uniform refinement, but with much less DoFs, as shown in Figure 25.

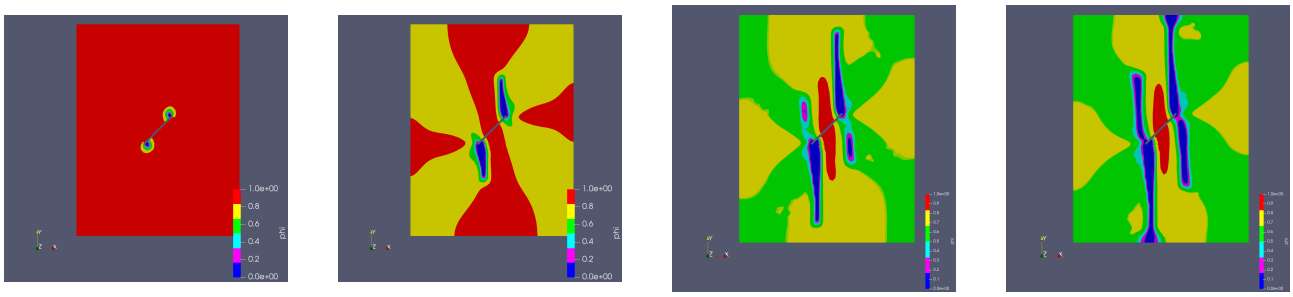

40th time step **100th** time step **135th** time step **142th** time step

Figure 23: Crack geometries of mixed-Freddi's splitting method under 0+1 mesh refinement in uniaxial compression test with an inclined notch

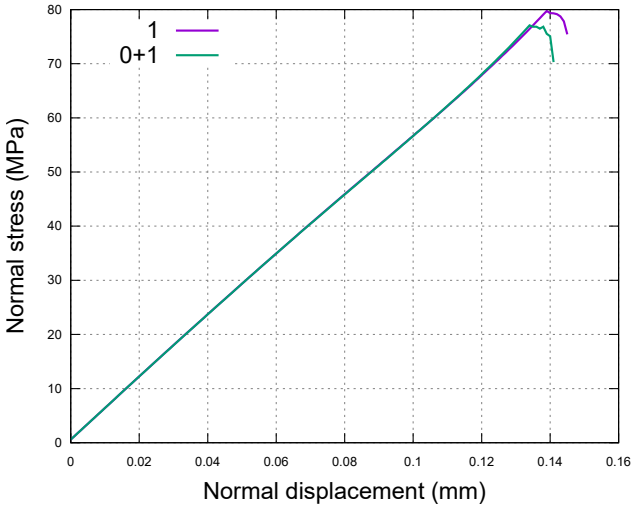

Figure 24: Load-displacement curves of mixed-Freddi's method under 0+0 and 0+1 refinement in uniaxial compression test with an inclined notch.

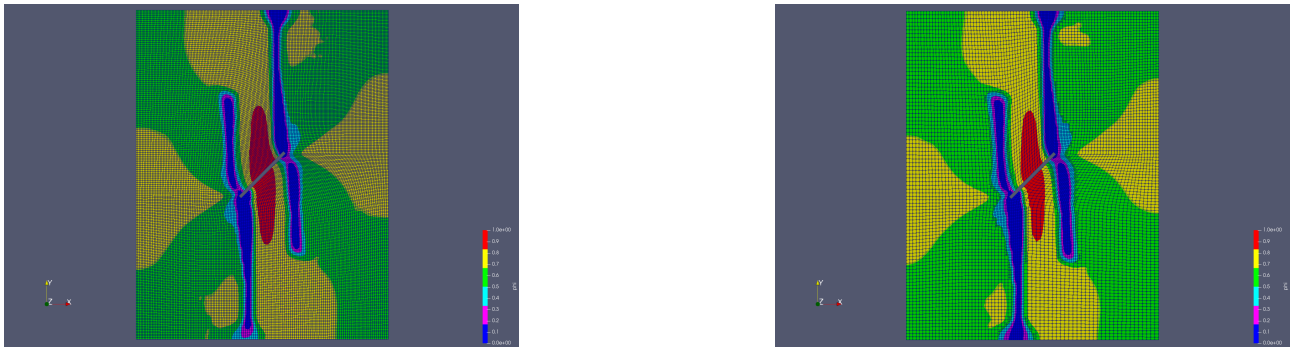

1+0 case 0+1 case

Figure 25: Mesh comparison between 1+0 and 0+1 cases using mixed-Freddi's method for uniaxial compression test with a single notch

6 Conclusions

In this work, we developed, on the basis of existing studies [32, 30, 29, 8, 14], a phase-field fracture model for capturing mixed-mode fracture propagation behavior. We used the phase-field fracture governing equations in [32], which incorporated the F-criterion into the classic phase-field fracture model. Specifically, we changed the reference frame of the energy splitting method proposed in [14] from principal strain coordinates to local fracture surface coordinates so that the crack-driving energy was further split into mode-I crack driving part and mode-II crack driving part. The fracture surface direction was determined based on the maximum-dissipation criterion from [8], but a simpler algorithm is proposed by us. Our computational framework was based on the implementation from [17, 18], where a quasi-monolithic scheme was used to solve the governing equations and adaptive mesh refinement and parallel computations were employed to reduce computation time. In this framework, a semi-smooth Newton method was used to solve the non-linear PDEs and treat the crack irreversibility. We hence provided the detailed algorithm to compute the right-hand-side and Jacobian matrix of Newton's method. Finally, to show the superiority of our new model over existing models, we used two classical numerical tests to demonstrate its numerical robustness and one practical test to demonstrate its physical soundness. We also showed the good compatibility of our new model with adaptive mesh refinement for reducing the computational cost. In the future, we are interested in extending the new model to three-dimensional scenarios so that more practical settings from engineering applications can be treated.

Acknowledgments

This work has been supported by the German Research Foundation, Priority Program 1748 (DFG SPP 1748) in the subproject *Structure Preserving Adaptive Enriched Galerkin Methods for Pressure-Driven 3D Fracture Phase-Field Models* with the project No. 392587580. The authors are also grateful for the financial support from the program of China Scholarships Council (No. 201806440069) and National Natural Science Foundation of China (No. 51490651).

References

References

[1] M. Ambati, T. Gerasimov, and L. De Lorenzis. A review on phase-field models of brittle fracture and a new fast hybrid formulation. *Computational Mechanics*, 55(2):383–405, 2015.

[2] L. Ambrosio and V. Tortorelli. On the approximation of free discontinuity problems. *Boll. Un. Mat. Ital. B*, 6:105–123, 1992.

[3] L. Ambrosio and V. M. Tortorelli. Approximation of functional depending on jumps by elliptic functional via t-convergence. *Communications on Pure and Applied Mathematics*, 43(8):999–1036, 1990.

[4] H. Amor, J.-J. Marigo, and C. Maurini. Regularized formulation of the variational brittle fracture with unilateral contact: Numerical experiments. *Journal of the Mechanics and Physics of Solids*, 57(8):1209–1229, 2009.

[5] B. K. Atkinson. *Fracture mechanics of rock*. Elsevier, 2015.

[6] S. Bandyopadhyay. Crack propagation studies of bulk polymeric materials in the scanning electron microscope. *Journal of materials science letters*, 3(1):39–43, 1984.

[7] B. Bourdin, G. A. Francfort, and J.-J. Marigo. Numerical experiments in revisited brittle fracture. *Journal of the Mechanics and Physics of Solids*, 48(4):797–826, 2000.

[8] E. C. Bryant and W. Sun. A mixed-mode phase field fracture model in anisotropic rocks with consistent kinematics. *Computer Methods in Applied Mechanics and Engineering*, 342:561–584, 2018.

[9] G. F. Carey and J. T. Oden. *Finite Elements. Volume III. Compuational Aspects*. The Texas Finite Element Series, Prentice-Hall, Inc., Englewood Cliffs, 1984.

[10] Y. Chen, Y. Jin, M. Chen, Z. Yi, and X. Zheng. Quantitative evaluation of rock brittleness based on the energy dissipation principle, an application to type ii mode crack. *Journal of Natural Gas Science and Engineering*, 45:527–536, 2017.

[11] J. Dong, M. Chen, Y. Jin, G. Hong, M. Zaman, and Y. Li. Study on micro-scale properties of cohesive zone in shale. *International Journal of Solids and Structures*, 163:178–193, 2019.

[12] M. Fan, T. Wick, and Y. Jin. A phase-field model for mixed-mode fracture. Proceedings of the 8$^{\text{th}}$ GACM Colloquium on Computational Mechanics for Young Scientists from Academia and Industry, August 28–30, 2019 in Kassel, Germany, 2019.

[13] G. A. Francfort and J.-J. Marigo. Revisiting brittle fracture as an energy minimization problem. *Journal of the Mechanics and Physics of Solids*, 46(8):1319–1342, 1998.

[14] F. Freddi and G. Royer-Carfagni. Regularized variational theories of fracture: a unified approach. *Journal of the Mechanics and Physics of Solids*, 58(8):1154–1174, 2010.

[15] F. Freddi and G. Royer-Carfagni. Variational fracture mechanics to model compressive splitting of masonry-like materials. *Annals of Solid and Structural Mechanics*, 2(2-4):57–67, 2011.

[16] A. A. Griffith. Vi. the phenomena of rupture and flow in solids. *Philosophical transactions of the royal society of london. Series A, containing papers of a mathematical or physical character*, 221(582-593):163–198, 1921.

[17] T. Heister, M. F. Wheeler, and T. Wick. A primal-dual active set method and predictor-corrector mesh adaptivity for computing fracture propagation using a phase-field approach. *Computer Methods in Applied Mechanics and Engineering*, 290:466–495, 2015.

[18] T. Heister and T. Wick. Parallel solution, adaptivity, computational convergence, and open-source code of 2d and 3d pressurized phase-field fracture problems. *PAMM*, 18(1):e201800353, 2018.

[19] M. Hintermüller, K. Ito, and K. Kunisch. The primal-dual active set strategy as a semismooth newton method. *SIAM Journal on Optimization*, 13(3):865–888, 2002.

[20] J. Huang, G. Chen, Y. Zhao, and R. Wang. An experimental study of the strain field development prior to failure of a marble plate under compression. *Tectonophysics*, 175(1-3):269–284, 1990.

[21] A. Ingraffea. *Discrete fracture propagation in rock: laboratory tests and finite element*. PhD thesis, Doctoral thesis, University of Colorado, Denver, Colorado, 1977.

[22] A. R. Ingraffea and F. E. Heuze. Finite element models for rock fracture mechanics. *International Journal for Numerical and Analytical Methods in Geomechanics*, 4(1):25–43, 1980.

[23] H. Lee and S. Jeon. An experimental and numerical study of fracture coalescence in pre-cracked specimens under uniaxial compression. *International Journal of Solids and Structures*, 48(6):979–999, 2011.

[24] K. Mang and T. Wick. Numerical methods for variational phase-field fracture problems. Lecture notes; Hannover : Institutionelles Repositorium der Leibniz Universität Hannover, July 2019.

[25] C. Miehe, M. Hofacker, and F. Welschinger. A phase field model for rate-independent crack propagation: Robust algorithmic implementation based on operator splits. *Computer Methods in Applied Mechanics and Engineering*, 199(45-48):2765–2778, 2010.

[26] C. Miehe, F. Welschinger, and M. Hofacker. Thermodynamically consistent phase-field models of fracture: Variational principles and multi-field fe implementations. *International Journal for Numerical Methods in Engineering*, 83(10):1273–1311, 2010.

[27] M. S. Paterson and T.-f. Wong. *Experimental rock deformation-the brittle field*. Springer Science & Business Media, 2005.

[28] B. Shen and O. Stephansson. Modification of the g-criterion for crack propagation subjected to compression. *Engineering Fracture Mechanics*, 47(2):177–189, 1994.

[29] C. Steinke and M. Kaliske. A phase-field crack model based on directional stress decomposition. *Computational Mechanics*, 63(5):1019–1046, 2019.

[30] M. Strobl and T. Seelig. A novel treatment of crack boundary conditions in phase field models of fracture. *Pamm*, 15(1):155–156, 2015.

[31] N. Y. Wong. *Crack coalescence in molded gypsum and Carrara marble*. PhD thesis, Massachusetts Institute of Technology, 2008.

[32] X. Zhang, S. W. Sloan, C. Vignes, and D. Sheng. A modification of the phase-field model for mixed mode crack propagation in rock-like materials. *Computer Methods in Applied Mechanics and Engineering*, 322:123–136, 2017.

[33] X. Zhang, C. Vignes, S. W. Sloan, and D. Sheng. Numerical evaluation of the phase-field model for brittle fracture with emphasis on the length scale. *Computational Mechanics*, 59(5):737–752, 2017.

[34] M. D. Zoback and J. D. Byerlee. The effect of microcrack dilatancy on the permeability of westerly granite. *Journal of Geophysical Research*, 80(5):752–755, 1975.